Revision 3

New insights into the control of visible gold fineness and deposition: A case study of the Sanshandao gold deposit (Jiaodong, China)

Hong-Wei Peng[1,2], Hong-Rui Fan[1,2,3*], Xuan Liu[4], Bo-Jie Wen[5], Yong-Wen Zhang[1,2], Kai Feng[1,2]

[1]*Key Laboratory of Mineral Resources, Institute of Geology and Geophysics, Chinese Academy of Sciences, Beijing 100029, China*

[2]*College of Earth and Planetary Sciences, University of Chinese Academy of Sciences, Beijing 100049, China*

[3]*Innovation Academy for Earth Science, Chinese Academy of Sciences, Beijing 100029, China*

[4]*GeoRessources Lab, Université de Lorraine, CNRS, CREGU, 54500 Vandoeuvre-lès-Nancy, France*

[5]*Institute of Mineral Resources, Chinese Academy of Geological Sciences, Beijing 100037, China*

*Corresponding author. E–mail: fanhr@mail.iggcas.ac.cn; Address: as above; Phone: (+86) 010 82998218; Fax: (+86) 10 62010846

ABSTRACT

Mineralogical distribution, textures, electron probe microanalysis of visible gold, laser ablation inductively coupled plasma mass spectrometry (LA-ICP-MS) trace element analysis of pyrite, and LA-multicollector (MC-)ICP-MS sulfur isotope analysis of sulfide minerals are examined in an ore zone extending obliquely to -4 km depth in the Sanshandao gold deposit (Jiaodong, China). We relate these results to the temporal and spatial ore forming processes in the deposit to further elucidate the controls on deposition of visible Au and fineness variation.

Two generations of Au mineralization are identified. The early generation is represented by beresitization and quartz-pyrite veins, in which visible Au grains are associated with pyrite (Py1 and Py2) and are characterized by high fineness (729-961; fineness = 1000×Au/(Au+Ag)). Py1 and Py2 are both enriched in Co, Ni and Bi, and depleted in As and Au. Texturally, gold and pyrite are pristine crystals, homogeneous in composition. These features are attributed to the sulfidation of the granitic wallrock (fluid rock interaction) that effectively destabilizes Au in the ore forming fluids during pyrite deposition. Fineness decreases continuously from 870 at -2650 m depth to 752 at -420 m depth. The Co and Ni contents of Py1 and Py2 decrease significantly from -4000 m to -420 m depth, whereas the As contents increase. The mean $\delta^{34}S$ values of Py1 increase from 10.5‰ to 11.8‰. The spatial variations are interpreted to be related to gradual cooling, decompression and an enhanced degree of fluid/rock

interaction with decreasing depth, which facilitated the initiation of visible gold mineralization at ca. -2700 m depth.

The late generation of Au mineralization is represented by quartz-polysulfide veins, in which visible Au grains are associated with multiple sulfide minerals (Py3, galena, chalcopyrite, arsenopyrite and sphalerite). It is characterized by low fineness (549-719), and heterogeneous textures with Ag-rich parts (218-421). Py3, occurring as the rim of pyrite grain are interpreted to form by replacement via a dissolution-reprecipitation reaction. Py3 is distinctly enriched in As (median of 10000 ppm) and Au (2.2 ppm), but depleted in Co, Ni and Bi. The $\delta^{34}S$ values of the polysulfide minerals decrease sharply by 4 to 5‰ at depths from -1909 to -1450 m depth. These features are interpreted to be generated by significant decompression and phase separation of fluid, where most ore elements (e.g. Au, Ag, As and base metal elements) are destabilized. Our study suggests that remobilization did not affect the generation of visible Au mineralization at Sanshandao.

Keywords: visible gold grain; fineness; *in-situ* pyrite trace elements; *in-situ* sulfide sulfur isotope; Sanshandao gold deposit; Jiaodong

INTRODUCTION

Visible Au, the product of Au super-saturation in ore-forming fluid, is the primary and crucial resource of Au in different types of Au deposits. There is complete Au-Ag solid solution and the composition is normally expressed as the Au fineness (1000 Au/(Au + Ag), by weight; Hough et al. 2009). The Au fineness shows different ranges in different deposits (Morrison et al. 1991), and was deemed to be an indicator of the ore-forming process (Pal'yanova 2008). In recent years, many attempts have been made to understand what factors control deposition and fineness of Au by physicochemical modeling, and it has been found to be complicatedly related to multiple-physicochemical conditions (Morrison et al. 1991; Gammons and Williams-Jones 1995; Pal'yanova 2008; Liang and Hoshino 2015). This complexity makes it difficult to directly correlate the Au fineness with the ore-forming process, and the factors which control the Au fineness range and variation in a deposit are poorly constrained. Numerous studies have proposed the crucial role of remobilization in concentrating Au sources and forming visible Au grains (e.g. Morey et al. 2008; Large et al. 2009, 2011; Sung et al. 2009; Cook et al. 2013; Fougerouse et al. 2016; and references therein). However, although remobilization is thought to be commonplace in Au deposits, its ability to produce the majority of observed features of visible Au is still in question.

Gold in a majority of deposits shows close temporal and spatial relationship with sulfide minerals, especially (arsenian) pyrite (Large et al. 2011;

Deditius et al. 2014; Kusebauch et al. 2019; and references therein). The co-occurrence with Au makes pyrite a good proxy for Au deposition processes. Pyrite composition and texture have been used to trace mineralization history and related physicochemical conditions in Au deposits (Morey et al. 2008; Large et al. 2009, 2011; Cook et al. 2013; Gregory et al. 2016; Román et al. 2019; and references therein). Specifically, the sulfur isotopic composition of sulfides can reflect the depositional condition of Au (e.g. f_{O_2} and pH; Ohmoto 1972; Seal 2006), as Au in hydrothermal solution is commonly transported as sulfide complexes of $AuHS^0$ and $Au(HS)_2^-$ (Benning and Seward 1996; Stefansson and Seward 2003; Williams-Jones et al. 2009). Here, we combine textural and geochemical information of pyrite and other sulfide minerals with fineness of visible Au grains to determine what processes and factors control the deposition and fineness variation of Au.

The Jiaodong Au district, containing more than 4000 t Au resources, is the largest and most important Au producing region in China (Zhu et al. 2015; and references therein). In the region, the two major types of Au deposit, disseminated- and quartz vein-type, are both characterized by visible Au mineralization. However, little attention has been paid to the ore-forming process responsible for the visible Au mineralization. Recently, *in situ* analyses of pyrite in quartz vein-type Au deposits have revealed coupled behavior of As and Au (As-poor and As-rich; Feng et al. 2018; Li et al. 2018), which contrasts with the invariant trace element patterns in disseminated-type deposit (Yang et

al. 2016), indicating different ore-forming events in Jiaodong.

The Sanshandao Au deposit is one of the largest disseminated-type deposit in Jiaodong. The existence of arsenopyrite at shallow level (ca. <-1000 m depth; Fan et al. 2003) suggests As-rich fluids, and may imply the two types of ore-forming mechanisms at this deposit. Recently, deep drill holes (deepest down to -4006.17 m) have revealed visible Au mineralization with large-tonnage sources (totaling more than 1000 t) extending obliquely downward along the ore-controlling fault (Song et al. 2019). The lack of arsenopyrite in deep samples (Zhang et al. 2014) suggests important spatial variation in mineralogy and geochemistry of the deposit. Hence, the Sanshandao Au deposit provides an excellent opportunity to investigate the integrated temporal and spatial ore-forming processes, and further provides key information on the processes and factors required for the deposition of large scale visible Au mineralization in the Sanshandao deposit and Jiaodong Au district.

THE SANSHANDAO DEPOSIT

The Sanshandao Au deposit is located in the west of the Jiaodong Peninsula, which is one of the most important Au-producing area in China, situated in the southeast margin of the North China Craton (Fig. 1a). The geology of the Jiaodong Au district is mainly comprised of Precambrian metamorphic basement rocks and three generations of Mesozoic magmatic intrusions including the late Jurassic Linglong biotite granites (160-150 Ma),

the early Cretaceous Guojialing granodiorite (130-126 Ma), and late Cretaceous Aishan granites (118-113 Ma) (Fig. 1a; Yang et al. 2012; Li et al. 2019). Gold deposits in Jiaodong occur as quartz veins and disseminated/stockwork types (Fan et al. 2003). They are mainly hosted by the Linglong and Guojialing granitoids and are strictly controlled by a NNE- to NE- trending fault system (Fig. 1a). Most of these Au deposits have a relatively uniform mineralization age of 126-117 Ma (Cai et al. 2018).

The Sanshandao Au deposit, one of the largest disseminated/stockwork type deposit in Jiaodong, has proved Au reserve of >260 t, and recent drill programs have discovered large Au resource at depths (>500t; Wen et al. 2015; Song et al. 2019). The ore bodies are mainly controlled by the NNE- trending and SE-dipping Sanshandao-Cangshang fault, and are mainly enclosed by Archean tonalite-trondhjemite-granodiorite gneisses (Jiaodong group rocks) and Linglong granite in the hanging wall and Guojialing granodiorite in the foot wall (Figs. 1b and 1c; Fan et al. 2003; Wen et al. 2016). The deposit is characterized by extensive hydrothermal alterations that extend ~6 km subvertically along the main fault, with Au ore bodies occurring in the footwall proximally to the fault. The drill holes show that K-feldspar alteration occurs distal to mineralization. This converts into sericitization (±silicification), and then, into beresitization proximal to the fault and marks the initiation of Au mineralization (Figs. 1c and 1d). The intensity and width of the alteration generally decreases with increasing depth along the fault, except for K-feldspar

alteration that maintains at largely stable thickness (Fig. 1c). The mineralogical and chemical evolution of the hydrothermal alteration are described in detail by Li et al. (2013).

PYRITE AND VISIBLE GOLD GENERATIONS

Gold mineralization at Sanshandao occurs as visible Au grains, and shows a close relationship with pyrite and other sulfide minerals. The Au mineralization can be subdivided into three different stages. In this contribution we define "visible Au grains" as individual crystals, generally larger than 1 μm, which can be observed under optical or scanning electron microscope.

Stage 1 beresitization (Fig. 1c) mainly consists of cataclastic quartz (35-45%), feldspar (5-10%), and relatively fine-grained sericite (30-40%) and pyrite (10-20%) (Fig. 2a and 2d). Pyrite in stage 1 (Py1) mainly occurs as euhedral to subhedral, cubic to polygonal grains, ranging in diameter between ca. 10 and 1000 μm, and shows close spatial association with sericite (Figs. 3a and 3b). Gold grains occur as small (<1 to 50 μm in diameter) inclusions in Py1 and fill in the grain boundaries of Py1 (Fig. 3a). There is no zonation and chemically heterogeneous texture observed under back-scattered electron (BSE) images for Py1 and the Au grains.

Stage 2 is characterized by quartz-pyrite veins. These appear as relatively curved veins in the sericitization, beresitization and K-feldspar zones (Figs. 1d; 2b, c, e). The veins consist mainly of quartz (35-55%), pyrite (40-60%) and

sericite (5-10%) (Fig. 2e). Pyrite (Py2) occurs as subhedural to anhedral grains with relatively large size up to millimeter level in length (Figs. 3c and 3d). Locally, fractures in Py2 are filled by galena, chalcopyrite, arsenopyrite and sphalerite of stage 3 (Figs. 3e and 3f). Gold grains of stage 2, <1 to 200 μm in size, fill microfractures and boundaries of Py2 grains and occur as inclusions in Py2 (Fig. 3c). Py2 and the Au grains do not exhibit any zonation and chemically heterogeneous texture under BSE images.

Stage 3 is marked by quartz-polysulfide veins that develop in the sericitization and beresitization zones, and superposes or crosscuts the quartz-pyrite veins (Figs. 2c and 2f). It mainly consists of quartz (35-50%), polysulfides (50-65%; galena, chalcopyrite, arsenopyrite, pyrite and sphalerite) and sericite (0-5%). Stage 3 pyrite is characterized by a distinct core-rim texture in BSE images, with a dark core (Py3cr) overgrown by a bright euhedral to subhedral rim (Py3; Figs. 3g and 3k). Other sulfide minerals inter-grow and co-precipitate with Py3, and can occur as fine-grained inclusions in Py3cr (Figs. 3g and 3k). Gold grains of this stage, varying largely in size (<1 to 500 μm in diameter), co-precipitate with the polysulfides and distribute in contact boundaries between polysulfide and pyrite (Figs. 3e-3j). Sometimes, they occur as inclusions with polysulfide minerals in Py3 (Fig. 7). In addition, some of the Au grains are marked by heterogeneous distribution of Au and Ag, with Ag-rich parts intergrown with Au-rich parts (Figs. 3h-3j). These features distinguish them from the Au grains of earlier stages.

Py1 and Py2 can be found at different depths (reaching -3700 m to -4000 m), and the early Au mineralization is observed in samples from the underground tunnel, ZK96-3, to ZK96-6 (down to ca. -2650 m; Fig. 1d). The polysulfide assemblages of stage 3 are concentrated at shallow levels, especially for Py3 and arsenopyrite, which are only observed in samples from the underground tunnels (-400 m and -800 m); in the deep area, only limited galena, chalcopyrite and sphalerite are developed. The late Au mineralization is also concentrated in shallow levels, with the deepest example observed at -1447.8 to -1449.8 m (samples of ZK96-3-53 and -54; Fig. 1d), in which argentite is co-precipitated with galena, chalcopyrite and Au grains (Fig. 3l).

SAMPLING AND ANALYTICAL METHODS

Sampling strategy

Representative ore samples were collected from surface to the depth of ca. -4km along the fault from underground tunnels and three drill cores (Figs. 1c and 1d). Samples of beresitization and quartz-pyrite veins were collected from -420 and -800 m depth and drill holes ZK96-3 (-1813 to -2025 m), ZK96-6 (-2516 to -2679 m) and ZK96-5 (-3437 and -3982 m; Fig. 1d). Samples of quartz-polysulfide veins were mainly found and collected from the underground tunnels (-420 and -800 m) and several samples from the drill hole ZK96-3 (-1447.8 to -1449.8 m; -1813 m; Fig. 1d).

Scanning electron microscope (SEM) imaging

Petrographic observation of sulfides and Au minerals were carried out using a Nova NanoSEM 450 field emission SEM at the Institute of Geology and Geophysics, Chinese Academy of Sciences (IGGCAS). Back-scattered electron (BSE) images were acquired with an accelerating voltage of 15 kV and a primary beam current of 20 nA. The instrument is equipped with an X-MAXN80 Energy Dispersive X-ray Spectrometer (EDS) detector, which is used for semiquantitative spot analyses and elemental mapping.

Electron microprobe analysis

Quantitative spot analyses of Au grains and pyrite were performed on a JEOL JXA-8100 electron microprobe at IGGCAS, which was operated with 20 kV accelerating voltage and a 10 nA beam current with a 1-3 μm spot diameter. Counting time for each element was 20 s on peak and 10 s on background. Calibration standards used were pyrite for S and Fe, chalcopyrite for Cu, sphalerite for Zn, galena for Pb, and alloy or pure metal for As, Co, Ni, Ag and Au. The detection limits for each element were S (111 ppm), Fe (120 ppm), Co (122 ppm), Ni (100 ppm), Cu (165 ppm), Zn (185 ppm), As (381 ppm), Ag (229 ppm), Au (506 ppm), and Pb (309 ppm).

LA-ICP-MS trace element analysis and mapping

Spot and mapping analyses of trace elements in pyrite were conducted with an Agilent 7700x ICP-MS equipped with a Coherent Compex-Pro 193 nm ArF excimer laser generator and an ASI RESOLution-LR-S155 laser microprobe equipped at the State Key Laboratory of Ore Deposit Geochemistry, Institute of

Geochemistry, Chinese Academy of Sciences. For spot analysis, the laser was set to a pulse frequency of 5 Hz, an energy intensity of 3 J/cm^2, and a diameter of 26 μm. During ablation, the sample cell was purged with an atmosphere of Ar (900 mL/min), and then, the ablated materials were transported by He (350 mL/min). Each spot analysis included an initial acquisition of background for approximately 30 s with laser off, followed by data acquisition of samples for 60 s. In the analytical session, a primary standard of STDGL3, a new series of the STDGL2b-2 (Danyushevsky et al. 2011), was used to calibrate the concentrations of chalcophile and siderophile elements. The lithophile elements were calibrated using GSE-1G and GSD-1G. MASS-1 was analyzed to monitor the analytical accuracy. When compared to preferred values, analytical error was predominantly within 10% (Table 1). For every 10 analyses of samples, the STDGL3 was measured at the beginning and end, with two measurements of GSE-1G and GSD-1G and one measurement of MASS-1. ICPDATACAL was used for data reduction (Liu et al. 2008), and Fe content of EPMA data was used as the internal standard.

Trace element mapping of pyrite were performed by parallel lines of ablation, using the same system. The line ablations were carried out using a spot size of 10 μm or 15 μm with a repetition rate of 10 Hz and a rastering speed of 7 μm/s. A set of elements (^{56}Fe, ^{59}Co, ^{60}Ni, ^{65}Cu, ^{66}Zn, ^{75}As, ^{77}Se, ^{95}Mo, ^{107}Ag, ^{109}Ag, ^{121}Sb, ^{125}Te, ^{197}Au, ^{208}Pb, ^{209}Bi) was chosen for analysis. The acquisition time was set to 0.006 s for most elements, and 0.009 s for ^{197}Au, ^{107}Ag and ^{109}Ag.

The total sweep time was ~0.3 s. The mapping of sulfides was initiated and also terminated with two line ablations of STDGL3, GSE-1G and GSD-1G, which were used to calibrate the concentrations of trace elements and to monitor the sensitivity drift, which was shown to be negligible.

LA-MC-ICP-MS sulfur isotope analysis

Sulfur isotope analyses of sulfides were carried out by LA-MC-ICP-MS at the State Key Laboratory of Geological processes and Mineral Resources, China University of Geosciences (Wuhan). A Nu Plasma II MC-ICP-MS equipped with a RESOlution S-155 193 nm excimer ArF laser ablation system was used. During experiments, the laser was set to a spot size of 33 μm, a repetition rate of 8Hz and an energy density of 3–4 J/cm^2. The analysis time for each spot was 65 s, comprising a 25 s measurement of background with laser off and a 40 s sample analysis with laser on. Sample-standard bracketing was used to determine the $\delta^{34}S$ values of the samples throughout the analytical sessions. An in-house pyrite standard (WS-1, natural pyrite from the Wenshan polymetallic skarn deposit in Yunnan Province of South China; Zhu et al. 2016), was used to calibrate the mass bias for S isotopes. The $\delta^{34}S_{V\text{-}CDT}$ values (+1.1‰ ± 0.2‰) of WS-1 were determined by SIMS at the Institute of Geochemistry, Chinese Academy of Geochemistry, Guangzhou (Zhu et al. 2016). The true sulfur isotope ratio was calculated by correction for instrumental mass bias by linear interpolation between the biases calculated from two neighboring standard analyses. Standards were analyzed before and after a suite of 5 to 8

spot analyses. In this study, the external precision was ca. ± 0.4‰ (2SD).

RESULTS

Fineness of visible gold grains

The fineness (1000*Au/(Au+Ag), by weight) of Au grains has been calculated based on EPMA results, with the detailed data in Supplemental Table S1. The Au grains associated with Py1 and Py2 (early generation) show a similar range of high fineness (729-961; Table 2). In the samples at depths of -420 and -800 m, Au grains have a range of fineness of 729 to 807 (mean=752; n=11) and 751 to 859 (mean=785; n=10), respectively. For depths from -1855 to-1897 m, the fineness range is 795 to 939, with an average of 855 (n=24). For depths between -2613 and -2650 m, the fineness ranges from 826 to 961, with an average of 870 (n=30). Hence, there is a tendency for fineness of early generation Au grains to increase with depth (Fig. 4).

The Au grains associated with polysulfide minerals (late generation) show much lower fineness (218-719) compared with the early generation (Table 2; Fig. 4). Gold grains from the depth of -420 m have fineness of 618 to 709 (mean =649; n=8), whereas those from the depth of -800 m range from 549 to 719 (mean=654; n=27). In the heterogeneous Au grains, the silver-rich parts have fineness of 218 to 421 (n=6), and the Au -rich parts have fineness of 634 to 696 (n=4). The deepest Au grains of the late generation occur at depths between -1447.8 and -1449.8 m and have fineness range from 623 to 693 (mean=670;

n=7).

Trace elements of pyrite

Pyrite of the three stages of mineralization have a range in trace metal contents, with Co, Ni and As showing the greatest variability; both Bi and Au content show moderate variability. The base metals Cu, Zn, Sb and Pb, as well as Ag, show similar ranges of content among the different pyrites. Following Gregory et al. (2019), median and median absolute deviation (MAD) values of the contents are utilized for data interpretations. The trace elemental data for pyrites are summarized in Table 3, and full data sets are provided in Supplemental Table S2.

Py1 is characterized by being enriched in Co (median of 46.0 ppm), Ni (19.6 ppm) and Bi (10.2 ppm), and depleted in As (512 ppm) and Au (0.1 ppm; Table 3; Fig. 5a). With depth decreasing from ca. -3700 m to -420 m, the median content of Co decreases from 247 to 2.6 ppm, with Ni decreasing from 618 to 2.5 ppm, and As increasing from 7.2 ppm to 864 ppm (Table 3; Figs. 5b-d).

Py2 also has relatively high contents of Co (median of 8.0 ppm), Ni (10.3 ppm) and Bi (2.4 ppm) and low contents of As (41.7 ppm) and Au (BDL) (Table 3; Fig. 5a). Similar to Py1, with decreasing depth from ca. -3700 m to -420 m, the median content of Co decreases from 1330 to 1.8 ppm, with Ni decreasing from 158 to 0.4 ppm, and As increasing from 3.5 ppm to 40.9 ppm (Table 3; Figs. 5b-d).

Py3 and Py3cr, which are developed at shallow level (-420 and -800 m),

are distinctly depleted in Co, Ni, and Bi compared to Py1 and Py2, with most spot analyses below detection limits (Table 3; Fig. 5a). Compared to other pyrites, Py3 is markedly enriched in As and Au, with median content are 10000 ppm and 2.2 ppm, respectively (Table 3; Fig. 5a).

Py1, Py2 and Py3cr show similar range of content ratios of Au/As, Au/Ag, Au/Cu and Au/Pb, which vary significantly and span over 3 to 4 orders of magnitude (Figs. 6a-d). By comparison, Py3 shows higher ratios of Au/Ag, Au/Cu and Au/Pb, due to its higher contents of Au (Figs. 6b-d), and has relatively high and consistent ratios of Au/As. For the ratios of Bi/Pb and Co/Ni, Py1 and Py2 show relatively consistent values lying between 10 and 10-1, whereas, Py3cr and Py3 span largely in the ratio of Bi/Pb and cluster for Co/Ni due to low concentrations (Figs. 6e-f).

Trace element mapping

Trace element mapping by LA-ICP-MS were conducted on two grains of Py3, one of which is shown in Fig. 7. The grain has a quite irregular boundaries between core (Py3cr) and rim (Py3), illustrated by the enrichment of As and Au in Py3 (Fig. 7b-c). Additionally, Py3 is slightly depleted in Ag and Cu relative to Py3cr (Figs. 7d-f), due to abundant micro-inclusions of galena and chalcopyrite in Py3cr (Fig. 7a). The other mapped grain shows similar core-rim trace element patterns (Fig. S1; detailed description given in the Supplemental Material S1).

Sulfur isotope composition of sulfides

Grains of Py1 have $\delta^{34}S$ ranging from 9.9 to 12.7‰, and the values increase slightly with decreasing depth. From -3600m to -420m, the mean $\delta^{34}S$ values increase from 10.5‰ to 11.1‰, 11.4‰ and 11.8‰ (Table 4; Fig. 8). Grains of Py2 have a predominant $\delta^{34}S$ range of 8.2 to 11.0‰, although several the deepest samples (> 3000 m) are significantly isotopically lighter (1.5 to 5.2‰). At a given depth, Py2 shows lower average $\delta^{34}S$ than Py1 (Table 4; Fig. 8).

A smaller number of grains of other sulfides (galena, chalcopyrite, sphalerite, arsenopyrite) were analyzed, which yield $\delta^{34}S$ generally lower than Py1 and Py2 from similar depths and overlapping the values of Py3 and Py3cr (Table 4; Fig. 8). Aside from the low $\delta^{34}S$ in the deep Py2 grains, sulfides show a general trend of higher $\delta^{34}S$ at shallower depths. Noticeably, polysulfides from -1448 m depth have much lower $\delta^{34}S$ than at other depths (Table 4; Fig. 8).

DISCUSSION

Two generations of visible Au mineralization

The combination of sulfide mineral assemblages and textures, fineness of Au grains, and trace element geochemistry of sulfides is consistent with the presence of two generations of Au mineralization at Sanshandao. The early generation include beresitization (stage 1) and quartz-pyrite vein (stage 2), where visible Au grains only show relationships with pyrite (Py1 and Py2). This Au is characterized by high fineness of 729-961 (mean=837; Table 2; Fig. 4),

dominated by native Au (>800; Hough et al. 2009). These Au grains and associated pyrites are all elementally homogeneous without significant internal zoning. The late generation corresponds to quartz-polysulfide veins (stage 3), where visible Au grains are associated with Py3 and polysulfide minerals. It is characterized by low fineness (mostly 549-719), and chemically heterogeneous textures with Ag-rich parts down to 218-421 (Table 2; Fig. 4). In addition, Py3 is distinct in occurring as the rim of pyrite grains and showing a core-rim texture. We suggest that the significant differences between the two generations reflect their distinctly different depositional mechanisms and physicochemical background (Morrison et al. 1991; Gammons and Williams-Jones 1995; Pal'yanova 2008).

Trace elemental evolution of pyrite

Py1 and Py2 are both relatively enriched in Co, Ni and Bi, and depleted in As and Au, (Table 3; Fig. 5a). The chemical features and chemically homogeneous textures features are similar to the disseminated pyrite within altered wall rocks (Peterson and Mavrogenes 2014; Yang et al. 2016), and the pyrite formed under non-boiling fluid conditions (Román et al. 2019). Furthermore, Py1 shows close spatial relationships with sericite within the beresitization zone (Fig. 3a), and the pyrite-quartz veins (Py2) develop irregular and curved boundaries within the hydrothermal alteration zones (Figs. 2a, 2b, 2e). These features indicate their successive genesis via fluid-rock interaction (sulfidation of wall rock).

Py1 and Py2 show concentrations of Co and Ni increasing with depth but As shows a reverse trend (Figs. 5b-d). The solubilities of chloride complexes of Co and Ni in fluids were determined to be strongly positively related to temperature (Migdisov et al. 2011; Liu et al. 2012), and specifically, a decrease of temperature from 300 to 200°C would lead to a decrease in Co solubility by more than two orders of magnitude. The Co and Ni contents of pyrite may not directly correlate with the temperature of environments, evidenced by some high Co and Ni contents in low temperature environments (Gregory et al. 2019), but, in the context of the Sanshandao deposit, the concentration variations are likely linked to change in temperature. With regard to As, Deditius et al. (2014) summarized a statistical equation of As content in pyrite with temperature: $C_{As} = 0.4785 \cdot e^{-0.0143T}$. According to it, the As content variations of Py1 from 240 ppm at ca. -3700 m to ca. 1000 ppm at -420 m (using mean contents here) correspond to temperature varying from ca. 500°C to 400°C. Although the estimated temperature is relatively high compared to the homogenization temperature of early fluid (250 to 400°C; Fan et al. 2003; Hu et al. 2013; Wen et al. 2016), a temperature decrease of <100°C is consistent with the variations in Co, Ni, and As with depth.

Py3 is characterized by enrichment in Au and As and marked depletion in Co, Ni and Bi (Table 3; Fig. 5a). The elemental mapping illustrates the irregular and sharp boundaries between core (i.e. Py3cr) and rim (i.e. Py3), with As-rich Py3 encroaching into Py3cr (Figs. 7a-c; S1). Py3cr shows overlapping trace

element contents and rations with Py1 and Py2, save for Co, Ni and Bi (Figs. 5a, 6). This suggests Py3 is formed by replacement of early pyrite (mainly Py2) via a dissolution-reprecipitation reaction, with the relic of early pyrite as core (Py3cr).

The dissolution-reprecipitation reaction is kinetically controlled by the relative solubility of the parent and product phase in fluid (Putnis 2002). For sulfide minerals, the relative solubilities mainly depend on the T, P, pH, f_{O2}, f_{S2}, and ligand concentration of fluid (Hemley et al. 1992; Reed and Palandri 2006; Sung et al. 2009). The sharp textural and compositional boundaries between the core and rim are likely reflective of sudden variations in fluid pressure (Peterson and Mavrogenes 2014). The abundance of sulfide micro-inclusions in Py3 and Py3cr, likely formed by preferential replacement of early pyrite by rapid percolation of fluid along fractures and a pore network (Fig. 7; Voute et al. 2019), is also indicative of rapid ingress of fluid, which can be readily achieved by decompression (Weatherley and Henley 2013). Meanwhile, significant decompression would further cause phase separation of H_2O-CO_2-NaCl fluid (Wilkinson and Johnston 1996; Velásquez et al. 2014), which is shown by the coexistence of CO_2-H_2O and H_2O-NaCl fluid inclusions in sphalerite of stage 3 (Hu et al. 2013; Wen et al. 2016). Moreover, decompression would promote higher solubilities of pyrite until fluid enters the two-phase field in temperature-composition space, where the solubilities would eventually decrease (Hemley et al. 1992). Hence, the formation of Py3 was likely controlled by

decompression. Additionally, under the phase separation background, As would be enriched in the fluid (Libbey and Williams-Jones 2016; Simmons et al. 2016), which contributed to coupled incorporation of As and Au into Py3 (Deditius et al. 2014; Kusebauch et al. 2019; Xing et al. 2019) and deposition of arsenopyrite (Pokrovski et al. 2002). Concomitant rapid cooling would lead to depletion of Co, Ni and Bi in fluid (Migdisov et al. 2011; Liu et al. 2012; Tooth et al. 2013) and the abundant deposition of base metal sulfide minerals (e.g. galena, chalcopyrite and sphalerite). The corresponding chemical features further indicate that Py3 and polysulfides are generated under significant decompression and resultant phase separation of fluid.

The significant decompression may be related to activities of secondary faults and expansion of new fractures (Xinli Au deposit, ca. 4km southwest to Sanshandao along Cangshang-Sanshandao fault; Yang et al. 2018). In contrast to the distribution of stage 1 and 2 at variable depths, stage 3 mineralization is concentrated on upper areas (<-1500 m depth). The difference in spatial distribution may relate to the more brittle behavior of rocks in the shallowest part of the deposit.

Sulfur isotopic evolution of pyrite and polysulfides

Sulfur isotopes in pyrite and polysulfides at Sanshandao vary temporally and spatially, reflecting a variation in physicochemical conditions as fluids migrated upward. The source of sulfur is not the focus in the present study and will not be discussed here, rather we will focus on the reasons for the isotopic

variation with depth.

The $\delta^{34}S$ values of Py1 (9.9 to 12.7‰; Table 4) is higher than Py2, of which most range from 8.2 to 11.0‰, with a minority of samples between 1.5 and 5.2‰ (Table 4; Fig. 8). However, the $\delta^{34}S$ difference may not be explained by deposition of Py1 leading to lower sulfur isotopes of remaining fluid, according to the -1.9‰ equilibrium $^{34}S/^{32}S$ fractionation between pyrite and H_2S in Syverson et al. (2015). The $\delta^{34}S$ values of Py1 are similar to the pyrite of disseminated-type deposits at Jiaodong (typically 9 to 12‰; Mao et al. 2008; Zhu et al. 2018), where sulfidation is the dominant Au and sulfide deposition mechanism. Py1 was generated after extensive fluid-rock interactions (i.e. K-feldspar alteration, sericitization and silicification), and from which CH_4 was derived (Fan et al. 2003; Wen et al. 2016), indicating a decrease of f_{O2} (Li et al. 2013). Hence, the parental fluid should correspond to lower $\delta^{34}S$ values in pyrite than those in Py1, since reduction would cause an increase of $\delta^{34}S$ value (Ohmoto 1972; Seal 2006). Quartz-pyrite (Py2) veins were emplaced in more interconnected spaces, and the sulfur isotopes of the fluid were less influenced by reduction, leading to lower $\delta^{34}S$ values in Py2 than in Py1.

Spatially, from ca. -3900 to -420 m, the $\delta^{34}S$ values of Py1 increase successively from 10.5‰ to 11.8‰, while, Py2 maintain at ca. 10.0‰ (Table 4; Fig. 8). The $\delta^{34}S$ increase is likely related to elevated degree of fluid-rock interaction, indicated by the more extensive hydrothermal alteration at relatively shallow depths (Figs. 1c and 1d; Fig. 9).

Low $\delta^{34}S$ values of Py2 (1.5 to 5.2‰) were obtained from several samples in hole ZK96-5 (-3437 and -3581 m depth), in rock with weak hydrothermal alterations (Figs. 1c and 1d). Wen et al. (2016) also obtained low $\delta^{34}S$ values ranging from 1.9 to 3.5‰ in bulk pyrite collected in weak K-feldspar alteration zone and Jiaodong group away from the main fault. Based on these observations, we suggest that the low $\delta^{34}S$ may derive from Precambrian basement rocks (-1.3 to 7.8‰; Wang et al. 2002).

The $\delta^{34}S$ values of polysulfides in stage 3 do not vary significantly with depths, but show noticeably lower values at hole ZK96-3 (-1448 to -1909 m depth; Table 4; Fig. 8). As discussed above, we interpret the deposition of polysulfides in the shallow portion of the deposit to have been triggered by decompression and phase separation of fluid, which led to sharp decrease of $\delta^{34}S$ values of hydrothermal minerals due to rapid loss of reduced gases (e.g. H_2, CH_4, H_2S) and the resultant increase in the ratio of S^{6+}/S^2 in residual fluid (Drummond and Ohmoto 1985; Mckibben and Eldridge 1990). Noticeably, the samples with the lowest $\delta^{34}S$ (ZK96-3-53 and -54) contain the observed deepest Au mineralization of the late generation, with co-deposition of argentite (Fig. 3l). Hence, we deduce that the pressure drop and phase separation of fluid might commence at the current depth of ca. -1500 m, supported by the large variation in fluid inclusion salinity between -1373 and -1666 m depth (Wen et al. 2016). In the shallower portion of the deposit, the $\delta^{34}S$ values of Py3 and polysulfides rise again, which was likely related to the deposition of galena and chalcopyrite

(Ohmoto 1972; Seal 2006).

Controls on deposition of visible Au grains and fineness variation

The high fineness (729-961) of early Au generation is similar to orogenic and Carlin-type Au deposits (typically 750-1000 in Morrison et al. 1991), where sulfidation of wall rock is the major mineralizing mechanism (Large et al. 2011; Kusebauch et al. 2019), consistent with Py1 and Py2 (Fig. 9). Consistent with the CO_2-H_2O-CH_4 fluid (Fan et al. 2003; Hu et al. 2013; Wen et al. 2016) and physicochemical conditions (weakly acidic and reducing) of stage 1 and 2, Au is transported as sulfur complexes ($Au(HS)^0$/$Au(HS)_2^-$), and Ag as chloride complexes ($AgCl_2^-$) at Sanshandao (Morrison et al. 1991; William-Jones et al. 2009; Pal'yanova 2008). Desulfidation of fluid for depositing Py1 and Py2 would destroy Au-S complexes, but have limited influence on Ag-Cl complexes, contributing to high fineness of Au grains (Morrison et al. 1991). Meanwhile, the production of CH_4 and decrease of f_{O2} further promotes the saturation and deposition of Au (Williams-Jones et al. 2009; Kusebauch et al. 2019). Likewise, the $As(OH)_3^0$ (Pokrovski et al. 2002; Kusebauch et al. 2019) and Cl^- complexes of Cu, Pb and Zn (Reed and Palandri 2006) would not be significantly affected, and were transported to shallow depths (Fig. 9). The markedly different fate of Au with other metals in the process also accounts for the 3 to 4 order of magnitude variation of Au/As, Au/Ag, Au/Cu and Au/Pb in Py1 and Py2 (Kusebauch et al. 2019; Fig. 6).

Noticeably, fineness of the early Au grains decreases from 870 to 752 with

decreasing depth from -2650 m to -420 m (Table 2; Figs. 4 and 9). The fineness variation is a complex function of mutiple physicochemical parameters (e.g., temperature, f_{S2}, f_{O2}, Cl^- concentration, pH and ∑Au/Ag) of fluid (Gammons and Williams-Jones 1995; Pal'yanova 2008). The stabilization of pyrite and sericite, and the saturation of Au at different depths suggest that no obvious change of f_{s2}, f_{O2}, pH and ∑Au/Ag of fluid has occurred. Hence, the decrease of Au fineness is likely attributed to a decrease of temperature (Fig. 9), since temperature is positively correlated with fineness (Gammons and Williams-Jones 1995; Pal'yanova 2008). Temperature decrease is also consistent with trace element variations in Py1 and Py2 with depth (i.e. Co, Ni and As). Although homogenization temperatures of fluid inclusions have found no obvious variation -4000 m to surface (Wen et al. 2016), the trapping temperatures corrected by pressure variations (ca. 110 MPa lithostatic pressure) correspond to a decrease of <100°C, consistent with the estimate based on As in Py1. Meanwhile, the enhanced degree of fluid-rock interaction, indicated by more extensive hydrothermal alterations (Fig. 9), was accompanied with increased reduction of the fluid, as evidenced by the presence of CH_4 in fluid inclusion from depth shallower than -3000 m (Wen et al. 2016). This is consistent with the initiation of visible Au mineralization at ca. -2700 m. Hence, from a spatial perspective, successive cooling (+decompression) and enhanced fluid-rock interaction controlled the deposition of Au grains and the variation of fineness (Fig. 9).

The late Au mineralization is marked by distinctly lower fineness (mostly 549-719 down to 218-421), similar to epithermal deposits (typically 440-1000 in Morrison et al. 1991). A pressure drop and phase separation of late mineralizing fluids would effectively destabilize Au-S and Ag-Cl complexes at the same time (Seward 1976; Morrison et al. 1991; Pal'yanova 2008; Williams-Jones et al. 2009), contributing to low fineness of visible Au grains (Fig. 9). In addition, the subsequent rapid cooling would drive more intense dissociation of Ag-Cl complexes and deposit Ag-rich grains (218-421 fineness). The lower fineness grains would be intimately intergrown with grains of higher fineness precipitated slightly earlier, leading to the chemical heterogeneity displayed by late Au mineralization. In the intense process, most ore elements in the fluid (e.g. As, Cu, Pb, Zn) were destabilized and saturated to deposit polysulfide minerals (Fig. 9). The coupled behavior of the elements in the process ensured Au incorporation with As to form invisible Au, which is also demonstrated by the consistent Au/As in Py3 (Fig. 6a; Kusebauch et al. 2019). From a spatial perspective, this ore-forming process focused on the shallow area in the deposit (Fig. 9).

Remobilization to form visible gold mineralization?

It has been commonly established that remobilization or redistribution of invisible Au in sulfides may result in formation of visible Au in orogenic Au deposits (Morey et al. 2008; Large et al. 2009, 2011; Sung et al. 2009; Cook et al. 2013; Fougerouse et al. 2016; Gregory et al. 2016; Cromie et al. 2018; and

567 references therein). In the present study, Au mineralization is dominant by
568 visible Au grains, except for the arsenian Py3 with a relatively high content of
569 Au. In addition to enrichment in As and Au, mobilization of trace elements
570 during dissolution reprecipitation reactions is also apparent in Py3 by depletion
571 of Co, Ni and Bi. However, it does not favor remobilization of Au to form
572 visible Au for following reasons. First, Py1 and Py2 have low concentration of
573 Au (Fig. 5a), with major analytical spots below detection limits, even if 100%
574 of the Au in Py1 and Py2 was remobilized, the mass of Au could not match the
575 large tonnage of the deposit (Yang et al. 2016). Second, Au mineralization in
576 early pyrite generations is also predominantly by visible Au, distributed in
577 fractures and grain boundaries of Py1 and Py2. The early pyrite generations do
578 not show any evidence of chemical remobilization (Figs. 3b and 3d). Finally,
579 visible Au of the late generation is significantly Ag-rich, in contrast to what
580 would be expected from remobilization (Zoheir et al. 2008; Liu et al. 2018; Li
581 et al. 2019), likely due to higher solubility and mobility of silver (Morrison et
582 al. 1991).
583

584 ## IMPLICATIONS

585 In this contribution, two generations of Au mineralization have been
586 recognized at Sanshandao. The early Au mineralization is characterized by Au
587 grains with high fineness. In contrast, late mineralization is distinct, with a
588 polysulfide mineral association and Au grains with low fineness. The two

589 generations of Au mineralization are attributed to sulfidation of wallrocks, and
590 decompression and phase separation of the fluid, respectively. The two
591 mechanisms are likely dominant in the disseminated-type deposits and quartz
592 vein-type deposits, respectively, which is observed in the Au deposits at
593 Jiaodong (e.g. Fan et al. 2003; Yang et al. 2016; Feng et al. 2018; Li et al.
594 2018). This study suggests that the two distinct drivers for mineralization can
595 act in one single deposit.

596 In this research, we relate the textural and chemical features of the pyrites
597 to their depositional mechanisms. The pyrite (Py1 and Py2) formed under
598 sulfidation process of wallrocks is characterized by chemically homogeneous
599 texture, with relatively high concentrations of Co and Ni and low concentrations
600 of As and Au. These pyrites are similar to pyrite of orogenic Au deposits
601 (Gregory et al. 2019), formed through sulfidation processes. In contrast, Py3
602 formed from phase separation of fluid (decompression). This generation occurs
603 as the rim of pyrite grains and is characterized by relatively high concentrations
604 of As and Au and low concentrations of Co and Ni. The abundant co-deposition
605 of low fineness Au, chalcopyrite and galena show the simultaneous significant
606 instabilities of Ag, Cu and Pb in the fluid. By comparison, the two different
607 pyrites are analogous to the pyrites formed under non-boiling and boiling fluids
608 as summarized by Román et al. (2019). As fluid conditions change, the behavior
609 of Co and Ni are generally the reverse of that exhibited by As, Ag, Au, as well
610 as Cu, Zn, Pb, and Sb, as recorded by pyrite (Peterson and Mavrogenes 2014;

611 Román et al. 2019). In brief, we stress that the linking between the textural and
612 chemical features of pyrite to the depositional mechanism can be applied
613 universally.

614 Trace elements and sulfur isotopes in sulfides have been explored in
615 numerous studies of different deposits (e.g. Peterson and Mavrogenes 2014;
616 Steadman et al. 2015; Gregory et al. 2016; LaFlamme et al. 2018; Voute et al.
617 2019), whereas, few studies have focused on the evolution with depth and
618 integrated these with the spatial variation of Au fineness. In this research, Co,
619 Ni and As concentrations of pyrite, sulfur isotopes and Au fineness changed
620 gradually with depth or temperature under steady fluid conditions (single-phase)
621 during early mineralization. When the fluid system changed suddenly into a
622 two-phase condition, the result was distinct depletion of Co and Ni and
623 enrichment of As in pyrite (Tardani et al. 2017; Román et al. 2019), and abrupt
624 decrease in $\delta^{34}S$ and Au fineness (Mckibben and Eldridge 1990; Morrison et al.
625 1991). Hence, the spatial variations of these elements and sulfur isotopes can
626 also provide critical information for the physicochemical conditions and
627 evolution of fluid system.

628

629 **ACKNOWLEDGMENTS**

630 We thank Xin Yan, Di Zhang, Ting-Guang Lan, Zhi-Hui Dai and Kui-Dong
631 Zhao for their help in SEM, EMP, LA-ICP-MS and LA-MC-ICP-MS analyses.
632 Xiao-Hui Jiang are thanked for her help on sampling. We are grateful to Daniel

Gregory and an anonymous referee for their constructive feedback that helped to improve an earlier draft of the manuscript, and associate editor Paul Tomascak for valuable suggestions and efficient editorial handling. This study was financially supported by the National Key Research and Development Program (No. 2016YFC0600105) and National Natural Science Foundation of China (41672094).

640 **REFERENCES CITED**

641 Benning, L.G., Seward, T. M. (1996) Hydrosulphide complexing of Au (I) in
642 hydrothermal solutions from 150–400 °C and 500–1500 bar. Geochimica
643 et Cosmochimica Acta, 60, 1849-1871.

644 Cai, Y.C., Fan, H.R., Santosh, M., Hu, F.F., Yang, K.F., Li, X.H. (2018)
645 Decratonic gold mineralization: evidence from the Shangzhuang gold
646 deposit, eastern North China Craton. Gondwana Research, 54, 1-22.

647 Cook, N.J., Ciobanu, C.L., Meria, D., Silcock, D., Wade, B. (2013)
648 Arsenopyrite-pyrite association in an orogenic gold ore: Tracing
649 mineralization history from textures and trace elements. Economic
650 Geology, 108, 1273-1283.

651 Cromie, P., Makoundi, C., Zaw, K., Cooke, D.R., White, N., Ryan, C. (2018)
652 Geochemistry of Au-bearing pyrite from the Sepon Mineral District, Laos
653 DPR, Southeast Asia: Implications for ore genesis. Journal of Asian Earth
654 Sciences, 164, 194-218.

655 Danyushevsky, L., Robinson, P., Gilbert, S., Norman, M., Large, R.,
656 McGoldrick, P., Shelley, M. (2011) Routine quantitative multi-element
657 analysis of sulphide minerals by laser ablation ICP-MS: Standard
658 development and consideration of matrix effects. Geochemistry-
659 Exploration Environment Analysis, 11, 51-60.

660 Deditius, A.P., Reich, M., Kesler, S.E., Utsunomiya, S., Chryssoulis, S.L.,
661 Walshe, J., Ewing, R.C. (2014) The coupled geochemistry of Au and As in

662 pyrite from hydrothermal ore deposits. Geochimica et Cosmochimica Acta,
663 140, 644-670.
664 Drummond, S.E., Ohmoto, H. (1985) Chemical evolution and mineral
665 deposition in boiling hydrothermal systems. Economic Geology, 80, 126-
666 147.
667 Fan, H.R., Zhai, M.G., Xie, Y.H., Yang, J.H. (2003) Ore-forming fluids
668 associated with granite hosted goldmineralization at the Sanshandao
669 deposit, Jiaodong gold province, China. Mineralium Deposita, 38, 739-750.
670 Feng, K., Fan, H.R., Hu, F.F., Yang, K.F., Liu, X., Shangguan, Y.N., Cai, Y.C.,
671 Jiang, P. (2018) Involvement of anomalously As-Au-rich fluids in the
672 mineralization of the Heilan'gou gold deposit, Jiaodong, China: Evidence
673 from trace element mapping and in-situ sulfur isotope composition.
674 Journal of Asian Earth Sciences, 160, 304-321.
675 Fougerouse, D., Micklethwaite, S., Tomkins, A.G., Mei, Y., Kilburn, M.,
676 Guagliardo, P., Fisher, L.A., Halfpenny, A., Gee, M., Paterson, D., Howard,
677 D.L. (2016) Gold remobilisation and formation of high grade ore shoots
678 driven by dissolution-reprecipitation replacement and Ni substitution into
679 auriferous arsenopyrite. Geochimica et Cosmochimica Acta, 178, 143-159.
680 Gammons, C.H., Williams-Jones, A.E. (1995) Hydrothermal geochemistry of
681 electrum: thermodynamic constraints. Economic Geology, 90, 420-432.
682 Gregory, D.D., Large, R.R., Bath, A.B., Steadman, J.A., Wu, S., Danyushevsky,
683 L., Bull, S. W., Holden P., Ireland T. R. (2016) Trace element content of

pyrite from the Kapai Slate, St. Ives gold district, Western Australia. Economic Geology, 111, 1297-1320.

Gregory, D.D., Cracknell, M.J., Large, R.R., McGoldrick, P., Kuhn, S., Maslennikov, V.V., Baker, M.J., Ivan Belousov, N.F., Figueroa M.C., Steadman, J.A., Fabris, A.J., Lyons, T.W. (2019) Distinguishing ore deposit type and barren sedimentary pyrite using laser ablation-inductively coupled plasma-mass spectrometry trace element data and statistical analysis of large data sets. Economic Geology 114, 771-786.

Hemley, J.J., Cygan, G.L., Fein, J.B., Robinson, G.R., D'Angelo, W.M. (1992) Hydrothermal ore-forming processes in the light of studies in rock-buffered systems; I, Iron-copper-zinc-lead sulfide solubility relations. Economic Geology, 87, 1-22.

Hough, R.M., Butt, C.R., Fischer-Bühner, J. (2009) The crystallography, metallography and composition of gold. Elements, 5, 297-302.

Hu, F.F., Fan, H.R., Jiang, X.H., Li, X.C., Yang, K.F., Mernagh, T. (2013) Fluid inclusions at different depths in the Sanshandao gold deposit, Jiaodong Peninsula, China. Geofluids, 13, 528-541.

Kusebauch, C., Gleeson, S.A., Oelze, M. (2019) Coupled partitioning of Au and As into pyrite controls formation of giant Au deposits. Science advances, 5, eaav5891.

LaFlamme, C., Sugiono, D., Thébaud, N., Caruso, S., Fiorentini, M., Selvaraja, V., Jeon, H., Voute, F., Martin L. (2018) Multiple sulfur isotopes monitor

706 fluid evolution of an Archean orogenic gold deposit. Geochimica et
707 Cosmochimica Acta, 222, 436-446.
708 Large, R.R., Danyushevsky, L., Hollit, C., Maslennikov, V., Meffre, S., Gilbert,
709 S., Bull, S., Scott, R., Embsbo, P., Thomas, H., Singh, B., Foster, J. (2009)
710 Gold and trace element zonation in pyrite using a laser imaging technique:
711 Implications for the timing of gold in orogenic and Carlin-style sediment-
712 hosted deposits. Economic Geology, 104, 635-668.
713 Large, R.R., Bull, S.W., Maslennikov, V.V. (2011) A carbonaceous sedimentary
714 source-rock model for Carlin-type and orogenic gold deposits. Economic
715 Geology, 106, 331-358.
716 Li, W., Cook, N.J., Ciobanu, C.L., Xie, G., Wade, B.P., Gilbert, S.E. (2019)
717 Trace element distributions in (Cu)-Pb-Sb sulfosalts from the Gutaishan
718 Au-Sb deposit, South China: Implications for formation of high fineness
719 native gold. American Mineralogist, 104, 425-437.
720 Li, X.C., Fan, H.R., Santosh, M., Hu, F.F., Yang, K.F., Lan, T.G. (2013)
721 Hydrothermal alteration associated with Mesozoic granite-hosted gold
722 mineralization at the Sanshandao deposit, Jiaodong gold province, China.
723 Ore Geology Reviews, 53, 403-421.
724 Li, X.H., Fan, H.R., Yang, K.F., Hollings, P., Liu, X., Hu, F.F., Cai, Y.C. (2018)
725 Pyrite textures and compositions from the Zhuangzi Au deposit,
726 southeastern North China Craton: implication for ore-forming processes.
727 Contributions to Mineralogy and Petrology, 173, 73.

728 Li, X.H., Fan, H.R., Hu, F.F., Hollings, P., Yang, K.F., Liu, X. (2019) Linking
729 lithospheric thinning and magmatic evolution of late Jurassic to early
730 Cretaceous granitoids in the Jiaobei Terrane, southeastern North China
731 Craton. Lithos, 324, 280-296.
732 Liang, Y., Hoshino, K. (2015) Thermodynamic calculations of Au_xAg_{1-x}–Fluid
733 equilibria and their applications for ore-forming conditions. Applied
734 Geochemistry, 52, 109-117.
735 Libbey, R.B., Williams-Jones, A.E. (2016) Relating sulfide mineral zonation
736 and trace element chemistry to subsurface processes in the Reykjanes
737 geothermal system, Iceland. Journal of Volcanology and Geothermal
738 Research, 310, 225-241.
739 Liu, A.L., Jiang, M.R., Ulrich, T., Zhang, J., Zhang, X.J. (2018) Ore genesis of
740 the Bake gold deposit, southeastern Guizhou province, China: Constraints
741 from mineralogy, in-situ trace element and sulfur isotope analysis of pyrite.
742 Ore Geology Reviews, 102, 740-756.
743 Liu, W., Migdisov, A., Williams-Jones, A. (2012) The stability of aqueous
744 nickel (II) chloride complexes in hydrothermal solutions: Results of UV–
745 Visible spectroscopic experiments. Geochimica et Cosmochimica Acta, 94,
746 276-290.
747 Liu, Y., Hu, Z., Gao, S., Xu, J., Gao, C., Chen, H. (2008) In situ analysis of
748 major and trace elements of anhydrous minerals by LA-ICP-MS without
749 applying an internal standard. Chemical Geology, 257, 34-43.

Mao, J.W., Wang, Y.T., Li, H.M., Pirajno, F., Zhang, C.Q., Wang, R.T. (2008) The relationship of mantle-derived fluids to gold metallogenesis in the Jiaodong Peninsula: evidence from D–O–C–S isotope systematics. Ore Geology Reviews, 33, 361-381.

McKibben, M.A., Eldridge, C.S. (1990) Radical sulfur isotope zonation of pyrite accompanying boiling and epithermal gold deposition: a SHRIMP study of the Valles Caldera, New Mexico. Economic Geology, 85, 1917-1925.

Migdisov, A.A., Zezin, D., Williams-Jones, A.E. (2011) An experimental study of cobalt (II) complexation in Cl^- and H_2S-bearing hydrothermal solutions. Geochimica et Cosmochimica Acta, 75, 4065-4079.

Morey, A.A., Tomkins, A.G., Bierlein, F.P., Weinberg, R.F., Davidson, G.J. (2008) Bimodal distribution of gold in pyrite and arsenopyrite: examples from the Archean Boorara and Bardoc shear systems, Yilgarn Craton, Western Australia. Economic Geology, 103, 599-614.

Morrison, G.W., Rose, W.J., Jaireth, S. (1991) Geological and geochemical controls on the silver content (fineness) of gold in gold-silver deposits. Ore Geology Reviews, 6, 333-364.

Ohmoto. H. (1972) Systematics of sulfur and carbon isotopes in hydrothermal ore deposits. Economic Geology, 67, 551-578.

Pal'yanova, G. (2008) Physicochemical modeling of the coupled behavior of gold and silver in hydrothermal processes: Gold fineness, Au/Ag ratios and

their possible implications. Chemical Geology, 255, 399-413.

Peterson, E.C., Mavrogenes, J.A. (2014) Linking high-grade gold mineralization to earthquake-induced fault-valve processes in the Porgera gold deposit, Papua New Guinea. Geology, 42, 383-386.

Pokrovski, G.S., Kara, S., Roux, J. (2002) Stability and solubility of arsenopyrite, FeAsS, in crustal fluids. Geochimica et Cosmochimica Acta, 66, 2361-2378.

Putnis, A. (2002) Mineral replacement reactions: from macroscopic observations to microscopic mechanisms. Mineralogical Magazine, 66, 689-708.

Reed, M.H., Palandri, J. (2006) Sulfide mineral precipitation from hydrothermal fluids. Reviews in Mineralogy and Geochemistry, 61(1), 609-631.

Román, N., Reich, M., Leisen, M., Morata, D., Barra, F., Deditius, A.P. (2019) Geochemical and micro-textural fingerprints of boiling in pyrite. Geochimica et Cosmochimica Acta, 246, 60-85.

Seal, R.R. (2006) Sulfur isotope geochemistry of sulfide minerals. Reviews in Mineralogy and Geochemistry, 61(1), 633-677.

Seward, T.M. (1976) The stability of chloride complexes of silver in hydrothermal solutions up to 350 °C. Geochimica et Cosmochimica Acta, 40, 1329-1341.

Simmons, S.F., Brown, K.L., Tutolo, B.M. (2016) Hydrothermal transport of

Ag, Au, Cu, Pb, Te, Zn, and other metals and metalloids in New Zealand geothermal systems: Spatial patterns, fluid-mineral equilibria, and implications for epithermal mineralization. Economic Geology, 111, 589-618.

Song, M.C., Song, Y.X., Ding, Z.J., Wei, X.F., Sun, S.L., Song, G.Z., Zhang, J.J., Zhang, P.J., Wang, Y.G. (2019) The discovery of the Jiaojia and the Sanshandao giant gold deposits in Jiaodong Peninsula and discussion on the relevant issues. Geotectonica et Metallogenia, 43, 92-110 (in Chinese with English abstract).

Steadman, J.A., Large, R.R., Meffre, S., Olin, P.H., Danyushevsky, L.V., Gregory, D.D., Belousov, I., Lounejeva, E., Ireland, T.R., Holden, P. (2015) Synsedimentary to early diagenetic gold in black shale hosted pyrite nodules at the Golden Mile deposit, Kalgoorlie, Western Australia. Economic Geology, 110, 1157-1191.

Stefánsson, A., Seward, T.M. (2003) Experimental determination of the stability and stoichiometry of sulphide complexes of silver (I) in hydrothermal solutions to 400 °C. Geochimica et Cosmochimica Acta, 67, 1395-1413.

Sung, Y.H., Brugger, J., Ciobanu, C.L., Pring, A., Skinner, W., Nugus, M. (2009) Invisible gold in arsenian pyrite and arsenopyrite from a multistage Archaean gold deposit: Sunrise Dam, Eastern Goldfields Province, Western Australia. Mineralium Deposita, 44, 765-791.

Syverson, D.D., Ono, S., Shanks, W.C., Seyfried Jr, W.E. (2015) Multiple sulfur

isotope fractionation and mass transfer processes during pyrite precipitation and recrystallization: an experimental study at 300 and 350 °C. Geochimica et Cosmochimica Acta, 165, 418-434.

Tardani, D., Reich, M., Deditius, A.P., Chryssoulis, S., Sánchez-Alfaro, P., Wrage J., Roberts M.P. (2017) Copper-arsenic decoupling in an active geothermal system: a link between pyrite and fluid composition. Geochimica et Cosmochimica Acta, 204, 179-204.

Tooth, B., Etschmann, B., Pokrovski, G.S., Testemale, D., Hazemann, J.L., Grundler, P.V., Brugger, J. (2013) Bismuth speciation in hydrothermal fluids: An X-ray absorption spectroscopy and solubility study. Geochimica et Cosmochimica Acta, 101, 156-172.

Velásquez, G., Béziat, D., Salvi, S., Siebenaller, L., Borisova, A.Y., Pokrovski, G.S., De Parseval, P. (2014) Formation and deformation of pyrite and implications for gold mineralization in the El Callao District, Venezuela. Economic Geology, 109, 457-486.

Voute, F., Hagemann, S.G., Evans, N.J., Villanes, C. (2019) Sulfur isotopes, trace element, and textural analyses of pyrite, arsenopyrite and base metal sulfides associated with gold mineralization in the Pataz-Parcoy district, Peru: implication for paragenesis, fluid source, and gold deposition mechanisms. Mineralium Deposita, 54, 1077-1100.

Wang, Y.W., Zhu, F.S., Gong, R.T. (2002) Tectonic isotope geochemistry–further study on sulphur isotope of Jiaodong Gold Concentration Area.

Gold, 23, 1-16 (in Chinese with English abstract).

Weatherley, D.K., Henley, R.W. (2013) Flash vaporization during earthquakes evidenced by gold deposits. Nature Geoscience, 6, 294-298.

Wen, B.J. (2015) Fluid evolution and ore genesis of typical gold deposits in the Northwest Jiaodong, Southeastern North China Craton: Unpublished Ph.D. thesis, Beijing, China, The University of Chinese Academy of Sciences, 164p (in Chinese with English abstract).

Wen, B.J., Fan, H.R., Hu, F.F., Liu, X., Yang, K.F., Sun, Z.F., Sun, Z.F. (2016) Fluid evolution and ore genesis of the giant Sanshandao gold deposit, Jiaodong gold province, China: constrains from geology, fluid inclusions and H–O–S–He–Ar isotopic compositions. Journal of Geochemical Exploration, 171, 96-112.

Wilkinson, J.J., Johnston, J.D. (1996) Pressure fluctuations, phase separation, and gold precipitation during seismic fracture propagation. Geology, 24, 395-398.

Williams-Jones, A.E., Bowell, R.J., Migdisov, A.A. (2009) Gold in solution. Elements, 5, 281-287.

Wilson, S.A., Ridley, W.I., Koenig, A.E. (2002) Development of sulfide calibration standards for the laser ablation inductively-coupled plasma mass spectrometry technique. Journal of Analytical Atomic Spectroscopy, 17, 406-409.

Xing, Y., Brugger, J., Tomkins, A., Shvarov, Y. (2019) Arsenic evolution as a

tool for understanding formation of pyritic gold ores. Geology, 47, 335-338.

Yang, K.F., Fan, H.R., Santosh, M., Hu, F.F., Wilde, S.A., Lan, T.G., Liu, Y.S. (2012) Reactivation of the Archean lower crust: Implications for zircon geochronology, elemental and Sr-Nd-Hf isotopic geochemistry of late Mesozoic granitoids from northwestern Jiaodong terrane, the North China craton. Lithos, 146, 112-127.

Yang, L., Zhao, R., Wang, Q., Liu, X., Carranza, E.J.M. (2018) Fault geometry and fluid-rock reaction: Combined controls on mineralization in the Xinli gold deposit, Jiaodong Peninsula, China. Journal of Structural Geology, 111, 14-26.

Yang, L.Q., Deng, J., Wang, Z.L., Guo, L.N., Li, R.H., Groves, D.I., Danyushevskiy, L., Zhang, C., Zheng, X.L., Zhao, H. (2016) Relationships between gold and pyrite at the Xincheng gold deposit, Jiaodong Peninsula, China: implications for gold source and deposition in a brittle epizonal environment. Economic Geology, 111, 105-126.

Zhang, C.Y. (2014) Pyrite genetic mineralogy and vertical contrast of the ultra-deep drill of Sanshandao gold deposit in Jiaodong: Unpublished M.Sc. thesis, Beijing, China, The University of Geosciences, 68p (in Chinese with English abstract).

Zhu, R.X., Fan, H.R., Li, J.W., Meng, Q.R., Li, S.R., Zeng, Q.D. (2015) Decratonic gold deposits. Science China Earth Sciences, 58, 1523-1537.

882 Zhu, Z.Y., Cook, N.J., Yang, T., Ciobanu, C., Zhao, K.D., Jiang, S.Y. (2016)
883 Mapping of sulfur isotopes and trace elements in sulfides by LA-(MC)-
884 ICP-MS: potential analytical problems, improvements and implications.
885 Minerals, 6, 110.
886 Zhu, Z.Y., Jiang, S.Y., Mathur, R., Cook, N.J., Yang, T., Wang, M., Ma, L.,
887 Ciobanu, C.L. (2018) Iron isotope behavior during fluid/rock interaction
888 in K-feldspar alteration zone–A model for pyrite in gold deposits from the
889 Jiaodong Peninsula, East China. Geochimica et Cosmochimica Acta, 222,
890 94-116.
891 Zoheir, B.A., El-Shazly, A.K., Helba, H., Khalil, K.I., Bodnar, R.J. (2008)
892 Origin and evolution of the Um Egat and Dungash orogenic gold deposits,
893 Egyptian Eastern Desert: evidence from fluid inclusions in quartz.
894 Economic Geology, 103, 405-424.
895

Figure captions

Figure 1. (a) Geologic map of Jiaodong Peninsula (after Fan et al., 2003). (b) Geologic map of the Sanshandao Au deposit (after Wen et al., 2016). (c) Cross section of the ZK96 prospecting line. (d) Three segments of drill holes of ZK96-3, ZK96-6 and ZK96-5 showing the details of hydrothermal alterations, veins and sampling information.

Figure 2. Photos of different types of mineralization and ore samples. (a) Beresitization and quartz-pyrite (Py2) vein. (b) Quartz-pyrite vein in beresitization zone. (c) Quartz-polysulfide vein and quartz-pyrite vein. (d) Hand specimen of beresitization containing cataclastic quartz and fine-grained sericite and Py1. (e) Curved quartz-pyrite vein in sericitization zone. (f) Quartz-pyrite vein and quartz-polysulfide vein in sericitization zone.

Figure 3. Representative photomicrographs of visible gold grains and related pyrite and other sulfide minerals. Numbers refer to fineness of individual spots on Au grains. (a) Reflected light image of visible Au grains distributed on boundaries of euhedral Py1. (b) Euhedral Py1 showing no zonation in BSE. (c) Reflected light image of visible Au grains in fractures of anhedral Py2. (d) Py2 showing no BSE zonation. (e) Galena (reflected light) co-precipitated with visible Au between pre-existing Py2. (f) Chalcopyrite (reflected light) co-precipitated with visible Au between pre-existing Py2. (g) Visible Au (reflected

light) co-precipitated with Py3, arsenopyrite and sphalerite. Inset shows BSE zonation that distinguishes Py3 and Py3cr. (h) Reflected light image of large, irregular-shaped Au grain, co-precipitated with arsenopyrite and galena. (i) EDS elemental map of grains in panel (h), showing heterogeneity in distribution of Au and Ag. (j) EDS elemental map of visible Au grain associated with Py3 and sphalerite (one area in Fig. 7a) showing heterogeneous texture in distribution of Au and Ag. (k) BSE image of Py3cr co-precipitated with polysulfides. Py3 appears as BSE-bright rim around inclusion-rich Py3cr core. (l) Argentite co-precipitated with chalcopyrite and galena in a sample of the deepest observed late generation Au mineralization.

Figure 4. Fineness of Au grains from early and late mineralization, relative to depth in the deposit. Grey arrow highlights trend of decreasing fineness of Au grains with decreasing depth.

Figure 5. LA-ICP-MS trace element results of pyrite. (a) Range and medians of trace element contents of different pyrite, with calculated mean content added for reference; the black horizontal bar is the mean detection limit. (b-c) Content variations of different pyrite with depths for the elements of Co (b), Ni (c) and As (d). Trace element concentrations below detection limit are plotted at half the detection limit values.

940 Figure 6. Scatter diagrams of trace element for different pyrites. (a) Au vs. As;
941 (b) Au vs. Ag; (c) Au vs. Cu; (d) Au vs. Pb; (e) Bi vs. Pb; (f) Co vs. Ni. Trace
942 element concentrations below detection limit are plotted at half the detection
943 limit values.

944

945 Figure 7. LA-ICP-MS elemental maps of pyrite with core (Py3cr) and rim (Py3).
946 (a) BSE image of the pyrite. (b-f) Concentration scales are in ppm (logarithmic
947 10^n, where n is given on scale).

948

949 Figure 8. The range of sulfur isotope values of different generations of pyrite
950 and polysulfide minerals relative to depth in the deposit. Significance of grey
951 arrows is explained in text.

952

953 Figure 9. Schematic model for the temporal and spatial evolution of the
954 hydrothermal system at Sanshandao Au deposit, showing the depositional
955 mechanisms, controlling factors, variation of fineness, migrations of metals,
956 pyrite formations and hydrothermal alteration zones.

957

958 **Table captions**

959 Table 1. LA-ICP-MS trace elements results of MASS-1.

960

961 Table 2. EPMA fineness results of visible Au grains from different stages and

962 depths at Sanshandao deposit.

963

964 Table 3. Summarized LA-ICP-MS analytical results of selective elements for
965 different pyrites from different depths at Sanshandao deposit.

966

967 Table 4. LA-MC-ICP-MS analytical results of sulfur isotopic composition of
968 different sulfide from different depths at Sanshandao deposit.

969

970 **Electronic Supplemental materials**

971 Supplemental Table S1. EPMA results of visible Au grains from different stages
972 and depths at Sanshandao deposit.

973

974 Supplemental Table S2. LA-ICP-MS analytical results different pyrites from
975 different depths at Sanshandao deposit.

976

Table1. LA-ICP-MS trace element results of MASS-1.

	Co	Ni	Cu	Zn	As	Ag	Sb	Te	Au	Pb	Bi
Mean (ppm)	59.5	94.9	131000	188000	58.1	58.6	73.8	17.1	52.1	78.4	71.4
S.D. (n=22)	3.8	5.5	6300	12000	2.6	2.8	6.6	1.1	4.2	8.5	3.0
Preferred Values[1]	60	97	134000	210000	65	50	60	15	47	68	60
Preferred Values[2]	67		134000	210000	65	67	55		47		7

S.D.= standard deviation

Preferred values1 is from the GeoRem database (http://georem.mpch-mainz.gwdg.de).

Preferred values2 is from Wilson et al. 2002.

Table 2. EPMA fineness results of visible gold grains from different stages and depths at Sanshandao deposit.

Sample No.	Associated sulfide	Depth (m)	Fineness
Early stage			
10S22	Py1	-420	773
10S22		-420	746
10S22		-420	754
10S16	Py2	-420	757
10S16		-420	807
10S16		-420	742
10S16		-420	729
10S16		-420	743
10S16		-420	731
10S16		-420	743
10S16		-420	749
		mean=752	
09S74	Py1	-800	772
09S74		-800	763
09S74		-800	779
09S74		-800	763
09S94		-800	776
09S94		-800	780
09S94		-800	751
09S37	Py2	-800	809
09S37		-800	802
09S37		-800	859
		mean=785	
ZK96-3-70	Py1	-1855	860
ZK96-3-70		-1855	852
ZK96-3-70		-1855	835
ZK96-3-70		-1855	925
ZK96-3-70		-1855	795
ZK96-3-72		-1866	817
ZK96-3-72		-1866	919
ZK96-3-72		-1866	921
ZK96-3-72		-1866	806
ZK96-3-72		-1866	858
ZK96-3-72		-1866	939
ZK96-3-75	Py2	-1880	853
ZK96-3-75		-1880	844
ZK96-3-75		-1880	941
ZK96-3-75		-1880	869
ZK96-3-75		-1880	826
ZK96-3-81		-1897	841
ZK96-3-81		-1897	824
ZK96-3-81		-1897	872
ZK96-3-81		-1897	821
ZK96-3-81		-1897	830
ZK96-3-81		-1897	828
ZK96-3-81		-1897	828
ZK96-3-81		-1897	822
		mean=855	
ZK96-6-82	Py1	-2627	828
ZK96-6-82		-2627	828
ZK96-6-82		-2627	850
ZK96-6-82		-2627	855
ZK96-6-82		-2627	851
ZK96-6-82		-2627	839
ZK96-6-82		-2627	919
ZK96-6-82		-2627	923
ZK96-6-82		-2627	869
ZK96-6-82		-2627	854
ZK96-6-82		-2627	826
ZK96-6-82		-2627	850
ZK96-6-82		-2627	857
ZK96-6-79	Py2	-2613	859
ZK96-6-79		-2613	869
ZK96-6-79		-2613	849
ZK96-6-79		-2613	846
ZK96-6-79		-2613	961
ZK96-6-84		-2636	917
ZK96-6-84		-2636	919
ZK96-6-84		-2636	895
ZK96-6-84		-2636	912
ZK96-6-84		-2636	868
ZK96-6-84		-2636	906
ZK96-6-84		-2636	878
ZK96-6-84		-2636	870
ZK96-6-85		-2650	850
ZK96-6-85		-2650	865
ZK96-6-85		-2650	831
ZK96-6-85		-2650	841
		mean=870	
Late stage			
10S23	Asp	-420	658
10S23	Asp	-420	644
10S23	Asp	-420	618
10S23	Asp-Sp	-420	709
10S23	Asp	-420	635
10S16	Py2-Gn	-420	638
10S16	Py2-Gn	-420	659
10S21	Py3-Sp	-420	634
		mean=649	
09S114-1	Py3-Sp	-800	608
09S114-1	Py3cr-Gn	-800	638
09S114-1	Py3cr	-800	638
09S114-1	Py3-Asp	-800	635
09S114-1	Py2-Asp	-800	660
09S114-2	Py2-Asp	-800	652
09S114-2	Py2-Asp	-800	626
09S114-2	Py2-Sp	-800	623
09S114-2	Py2-Gn	-800	588
09S114-2	Py2-Sp-Asp	-800	645
09S114-2	Py2-Sp-Gn	-800	630
09S114-2	Py2-Sp-Gn	-800	640
09S92	Py2-Gn	-800	624
09S92	Py2-Gn	-800	686
09S92	Py2-Gn	-800	686
09S92	Py2-Gn	-800	683
09S92	Py2-Gn	-800	549
09S92	Py2-Gn	-800	654
09S92	Py2-Gn	-800	684
09S92	Py2-Sp	-800	719
09S92	Py2-Sp	-800	719
09S93	Py2-Ccp	-800	666
09S93	Py2-Ccp	-800	643
09S93	Py2-Ccp	-800	698
09S119	Py2-Gn-Asp	-800	696
09S119	Py2-Gn-Asp	-800	689
09S119	Py2-Gn-Asp	-800	673
		mean=654	
ZK96-3-53	Ccp	-1448	672
ZK96-3-53	Py2-Ccp	-1448	667
ZK96-3-53	Py2-Ccp	-1448	623
ZK96-3-53	Py2-Ccp	-1448	687
ZK96-3-53	Py2-Ccp	-1448	680
ZK96-3-54	Py2-Ccp	-1448	665
ZK96-3-54	Py2-Ccp	-1448	693
		mean=670	
10S21	Py3-Sp	-420	421
09S114-1	Py2-Gn-Asp	-800	263
09S119	Py2-Gn-Asp	-800	348
09S119	Py2-Gn-Asp	-800	218
09S119	Py2-Gn-Asp	-800	233
09S119	Py2-Gn-Asp	-800	417
		mean=317	

Table 3. Summarized LA-ICP-MS analytical results of selective elements for different pyrites from different depths at Sanshandao deposit.

	Co	Ni	Cu	Zn	As	Ag	Sb	Te	Au	Pb	Bi
Py1 (-3537 ~ -3739m; n=5)											
Median	247	617	34.1	bdl	7.2	6.8	0.7	bdl	bdl	76.9	0.5
MAD	154	523	33.6	1.2	4.5	2.1	0.7	0.7	0.1	37.9	0.5
Min	92.5	93.9	bdl	bdl	2.7	bdl	bdl	bdl	bdl	bdl	bdl
Max	2770	3900	294	11.6	671	11.6	3.6	20.0	0.3	122	61.4
Py1 (-2516 ~ -2627m; n=8)											
Median	94.0	507	17.5	bdl	253	4.8	0.2	4.7	0.1	116	44.4
MAD	74.7	87.4	7.2	0.2	176	4.6	0.1	4.0	0.1	56.3	37.3
Min	19.3	18.6	bdl	bdl	4.9	bdl	bdl	bdl	bdl	1.0	2.7
Max	420	594	39.8	3.0	506	18.8	1.6	24.1	1.6	172	99.2
Py1 (-1855 ~ -1875m; n=8)											
Median	29.0	3.1	bdl	bdl	894	bdl	bdl	bdl	bdl	1.0	0.9
MAD	22.2	1.7	0.1	0.2	827	0.1	0.0	0.3	0.0	1.0	0.8
Min	0.6	0.8	bdl	bdl	11.4	bdl	bdl	bdl	bdl	bdl	0.1
Max	92.0	83.5	3.8	bdl	2610	2.1	0.2	4.7	0.5	9.0	23.5
Py1 (-420 ~ -800m; n=13)											
Median	2.6	2.5	3.2	bdl	864	2.2	0.2	4.4	0.1	8.7	10.6
MAD	2.5	2.3	1.3	0.2	357	1.9	0.2	3.6	0.1	7.4	6.2
Min	0.1	bdl	bdl	bdl	1.7	bdl	bdl	bdl	bdl	0.5	0.1
Max	171	222	26.1	7.0	2500	9.0	3.3	16.7	0.6	65.7	32.7
Py1 (all: -420 ~ -3739m; n=33)											
Median	46.0	19.6	3.2	bdl	512	2.1	0.2	2.5	0.1	8.7	10.2
MAD	45.2	19.4	2.8	0.3	460	2.0	0.1	2.0	0.1	8.2	9.6
Min	0.1	bdl	bdl	bdl	1.7	bdl	bdl	bdl	bdl	bdl	bdl
Max	2770	3900	294	11.6	2610	18.8	3.6	24.1	1.6	172	99.2
Py2 (-3633 ~ -3798m; n=8)											
Median	1330	158	0.8	bdl	3.5	bdl	bdl	bdl	bdl	0.6	1.0
MAD	1100	25.2	0.5	0.2	3.0	0.0	0.0	0.2	0.0	0.5	0.9
Min	83.5	64.8	bdl	bdl	bdl	bdl	bdl	bdl	bdl	bdl	bdl
Max	2900	257	24.9	1.8	28.4	8.5	1.4	21.5	0.3	254	55.0
Py2 (-2613 ~ -2680m; n=8)											
Median	14.8	28.9	6.6	bdl	90.4	3.7	0.1	7.4	0.6	29.2	17.6
MAD	6.2	10.1	6.0	0.3	28.6	3.5	0.1	5.1	0.5	27.9	16.1
Min	5.9	2.1	0.7	bdl	14.3	0.1	bdl	bdl	bdl	0.8	0.4
Max	103	92.9	36.2	1.8	252	16.3	0.8	37.7	1.2	307	91.5
Py2 (-1448 ~ -1909m; n=9)											
Median	5.5	1.7	bdl	bdl	64.3	0.3	bdl	bdl	bdl	0.7	8.7
MAD	2.5	1.5	0.1	0.2	62.2	0.3	0.0	0.5	0.0	0.6	8.6
Min	0.3	bdl	bdl	bdl	1.1	bdl	bdl	bdl	bdl	bdl	0.0
Max	12.2	46.7	8.4	3.8	1220	19.8	1.8	2.0	0.8	35.6	28.8
Py2 (-420 ~ -800m; n=20)											
Median	1.8	0.4	8.8	1.4	40.9	5.7	0.7	bdl	bdl	14.3	1.1
MAD	1.8	0.2	8.2	0.8	31.7	5.6	0.6	0.4	0.0	11.9	1.1
Min	bdl	bdl	bdl	bdl	4.9	bdl	bdl	bdl	bdl	0.1	bdl
Max	21.0	34.5	83.0	63.7	706	76.9	4.4	6.1	0.2	98.4	16.6
Py2 (all: -420 ~ -3798m; n=45)											

Median	8.0	10.3	1.7	bdl	41.7	2.6	0.2	bdl	bdl	5.4	2.4
MAD	7.7	10.1	1.5	0.4	38.1	2.5	0.1	0.4	0.0	5.3	2.3
Min	bdl	bdl	bdl	bdl	bdl	bdl	bdl	bdl	bdl	bdl	bdl
Max	2900	257	83.0	63.7	1220	76.9	4.4	37.7	1.2	307	91.5
Py3cr (-420 ~ -800m; n=24)											
Median	bdl	bdl	4.6	1.6	8.6	0.9	0.8	bdl	bdl	14.1	bdl
MAD	0.0	0.0	4.3	0.9	8.1	0.8	0.7	0.2	0.0	13.5	0.0
Min	bdl	bdl	bdl	bdl	bdl	bdl	bdl	bdl	bdl	bdl	bdl
Max	0.3	bdl	169	75.9	446	41.7	28.6	bdl	0.6	189	0.2
Py3 (-420 ~ -800m; n=29)											
Median	bdl	bdl	2.0	1.1	10000	0.8	1.2	bdl	2.2	7.6	bdl
MAD	0.0	0.0	1.2	0.5	2230	0.6	0.9	0.2	1.3	6.0	0.0
Min	bdl	bdl	bdl	bdl	1700	bdl	bdl	bdl	0.2	bdl	bdl
Max	1.5	1.1	25.6	9.5	16300	15.2	8.5	bdl	19.6	60.4	0.1

MAD = median absolute deviation

bdl = below detection limit

Table 4. LA-MC-ICP-MS analytical results of sulfur isotopic composition of different sulfide from different depths at Sanshandao deposit.

Sample No.	Depth (m)	$^{34}S/^{32}S$	$\delta^{34}S$‰
	Py1		
ZK96-5-177	-3537	0.049571	9.9
ZK96-5-177	-3537	0.049592	10.5
ZK96-5-177	-3537	0.049590	10.4
ZK96-5-177	-3537	0.049570	10.1
ZK96-5-177	-3537	0.049574	10.0
ZK96-5-216	-3739	0.049579	10.1
ZK96-5-216	-3739	0.049633	11.2
ZK96-5-216	-3739	0.049631	11.2
ZK96-5-216	-3739	0.049587	10.3
ZK96-5-216	-3739	0.049571	10.0
ZK96-5-216	-3739	0.049653	11.2
ZK96-5-218	-3748	0.049634	10.8
ZK96-5-218	-3748	0.049637	10.9
		mean = 10.5	
ZK96-6-72	-2516	0.049638	11.1
ZK96-6-72	-2516	0.049653	11.4
ZK96-6-72	-2516	0.049657	11.5
ZK96-6-72	-2516	0.049622	10.8
ZK96-6-82	-2627	0.049614	10.8
ZK96-6-82	-2627	0.049643	11.8
ZK96-6-82	-2627	0.049645	11.1
ZK96-6-82	-2627	0.049601	10.4
		mean = 11.1	
ZK96-3-70	-1855	0.049618	10.5
ZK96-3-70	-1855	0.049633	10.9
ZK96-3-70	-1855	0.049659	12.1
ZK96-3-72	-1866	0.049628	10.6
ZK96-3-72	-1866	0.049668	11.4
ZK96-3-72	-1866	0.049708	12.2
ZK96-3-74	-1875	0.049657	11.9
ZK96-3-74	-1875	0.049645	11.5
		mean = 11.4	
09S74	-800	0.049662	11.8
09S74	-800	0.049673	12.0
09S74	-800	0.049657	11.7
09S94	-800	0.049631	11.3
09S94	-800	0.049631	11.3
09S94	-800	0.049633	11.3
10S22	-420	0.049731	12.7
10S22	-420	0.049656	11.8
10S22	-420	0.049668	12.1
		mean = 11.8	
ZK96-5-185	-3581	0.049343	4.9
ZK96-5-185	-3581	0.049358	5.2
ZK96-5-185	-3581	0.049350	5.1
ZK96-5-169	-3437	0.049221	2.5
ZK96-5-169	-3437	0.049220	2.4
ZK96-5-169	-3437	0.049291	3.9
ZK96-5-169	-3437	0.049236	2.7
ZK96-5-169	-3437	0.049256	3.2
ZK96-5-169	-3437	0.049230	1.7
ZK96-5-169	-3437	0.049223	1.6
ZK96-5-169	-3437	0.049222	1.5
		mean = 3.1	
ZK96-6-79	-2613	0.049586	9.7
ZK96-6-79	-2613	0.049548	9.5
ZK96-6-79	-2613	0.049619	10.9
ZK96-6-84	-2636	0.049597	10.3
ZK96-6-84	-2636	0.049589	10.3
ZK96-6-86	-2652	0.049585	10.2
ZK96-6-86	-2652	0.049604	9.6
ZK96-6-88	-2680	0.049608	9.7
ZK96-6-88	-2680	0.049605	11.0
		mean = 10.1	
ZK96-3-53	-1448	0.049610	10.0
ZK96-3-53	-1448	0.049607	9.9
ZK96-3-66	-1813	0.049600	9.7
ZK96-3-66	-1813	0.049553	9.7
ZK96-3-74	-1875	0.049558	9.9
ZK96-3-74	-1875	0.049554	9.8
ZK96-3-81	-1897	0.049509	9.1
ZK96-3-81	-1897	0.049510	9.1
ZK96-3-81	-1897	0.049577	10.5
ZK96-3-82	-1909	0.049591	10.7
ZK96-3-82	-1909	0.049535	9.6
ZK96-3-82	-1909	0.049641	10.2
		mean = 9.8	
09S92	-800	0.049583	10.0
09S92	-800	0.049569	9.7
09S92	-800	0.049567	9.7
09S92	-800	0.049583	9.8
09S135	-800	0.049619	10.9
09S135	-800	0.049620	10.9
10S16	-420	0.049616	10.4
10S16	-420	0.049622	10.5
10S16	-420	0.049603	10.1
09S114-1	-800	0.049628	10.4
09S114-1	-800	0.049621	10.3
09S114-1	-800	0.049626	10.5
09S114-1	-800	0.049641	10.8
09S114-1	-800	0.049611	10.2
09S114-1	-800	0.049633	10.6
09S114-1	-800	0.049626	10.3
09S114-1	-800	0.049635	10.4
09S114-1	-800	0.049629	10.8
09S114-1	-800	0.049634	10.9
09S25	-800	0.049585	9.6
09S25	-800	0.049605	10.0
09S25	-800	0.049602	9.9
09S25	-800	0.049598	9.9
09S25	-800	0.049597	9.8
09S25	-800	0.049601	10.1
09S25	-800	0.049611	10.3
09S25	-800	0.049609	10.3
10S21	-420	0.049623	10.5
10S21	-420	0.049616	10.2
10S21	-420	0.049660	11.1
		mean = 10.3	
	Gn		
ZK96-5-179	-3551	0.049471	6.7
ZK96-5-179	-3551	0.049461	6.5
ZK96-6-86	-2652	0.049476	7.2
ZK96-6-86	-2652	0.049487	7.6
ZK96-3-53	-1448	0.049238	3.5
ZK96-3-53	-1448	0.049338	4.4
ZK96-3-66	-1813	0.049362	4.9
09S92	-800	0.049421	6.7
09S92	-800	0.049434	7.0
10S16	-420	0.049465	7.3
10S16	-420	0.049459	7.3
	Ccp		
ZK96-6-86	-2652	0.049545	8.4
ZK96-6-86	-2652	0.049505	8.1
ZK96-3-53	-1448	0.049332	5.5
ZK96-3-53	-1448	0.049338	5.6
ZK96-3-53	-1448	0.049350	5.8
ZK96-3-66	-1813	0.049511	8.8

Py2			
ZK96-5-175	-3522	0.049560	9.7
ZK96-5-175	-3522	0.049541	9.3
ZK96-5-175	-3522	0.049574	10.0
ZK96-5-179	-3551	0.049518	9.0
ZK96-5-179	-3551	0.049528	9.2
ZK96-5-183	-3566	0.049638	10.1
ZK96-5-183	-3566	0.049581	10.2
ZK96-5-195	-3633	0.049563	9.8
ZK96-5-195	-3633	0.049555	9.6
ZK96-5-218	-3748	0.049511	8.6
ZK96-5-218	-3748	0.049506	8.5
ZK96-5-218	-3748	0.049498	8.2
ZK96-5-227	-3798	0.049551	9.6
ZK96-5-227	-3798	0.049578	10.1
ZK96-5-227	-3798	0.049573	10.0
ZK96-5-227	-3798	0.049575	10.0
ZK96-5-244	-3982	0.049580	10.2
ZK96-5-244	-3982	0.049556	9.7
ZK96-5-244	-3982	0.049574	10.0
ZK96-5-244	-3982	0.049516	8.8
ZK96-5-244	-3982	0.049586	10.3
		mean = 9.6	

10S16	-420	0.049599	10.0
10S23	-420	0.049572	9.5
10S23	-420	0.049598	10.5
		mean = 10.2	

Py3cr			
09S114-1	-800	0.049561	9.0
09S114-1	-800	0.049570	9.2
09S114-1	-800	0.049584	9.5
09S114-1	-800	0.049575	9.4
09S114-1	-800	0.049560	9.1
09S114-1	-800	0.049585	9.6
09S114-1	-800	0.049561	8.9
09S114-1	-800	0.049559	8.9
09S114-1	-800	0.049591	10.0
09S114-1	-800	0.049585	9.9
09S25	-800	0.049541	8.7
09S25	-800	0.049545	8.8
09S25	-800	0.049538	8.6
09S25	-800	0.049555	9.2
10S21	-420	0.049586	9.7
10S21	-420	0.049565	9.2
10S21	-420	0.049589	9.6
		mean = 9.3	

ZK96-3-66	-1813	0.049514	8.0
ZK96-3-82	-1909	0.049546	9.5
ZK96-3-82	-1909	0.049569	10.0
09S92	-800	0.049613	10.8
10S16	-420	0.049574	9.7

Sp			
ZK96-3-53	-1448	0.049372	6.2
ZK96-3-53	-1448	0.049358	6.0
09S114-1	-800	0.049601	10.5
09S114-1	-800	0.049572	9.9
09S114-1	-800	0.049563	9.7
10S23	-420	0.049584	10.2
10S23	-420	0.049569	9.9

Apy			
09S114-1	-800	0.049597	9.7
09S114-1	-800	0.049592	10.0
09S25	-800	0.049578	9.4
09S25	-800	0.049566	9.2
09S25	-800	0.049577	9.4
10S23	-420	0.049596	10.5
10S21	-420	0.049595	9.9

a

Bohai Sea
Penglai
China
Jiaodong Peninsula
800km
Xincheng
Jiaojia
Sanshandao
Cangshang
Linglong
Yantai
Weihai
Muping
Zhaoyuan
Qixia
Denggezhuang
Wendeng
Laizhou
Yingezhuang
Jinqingding
Jiaobei terrane
Tan-Lu Fualt zone
Rushan
SuLu Belt
JiaoLai Basin
Pingdu
N
0
30
kilometers

b

N
Sanshandao-Cangshang fault
ZK96-4
ZK96-3
ZK96-6
ZK96-5
Line 96
F1
F2
F3
Bohai Sea
1km

c

124°07′
ZK96-4
ZK96-3
ZK96-6
ZK96-5
Elevation/m
0
-400
-800
-1200
-1600
-2000
-2400
-2800
-3200
-3600
-4000
①
②
③
1856.01m
2025.28m
2755.70m
4006.17m
200m

d

①
-1409m
#53
-1500m
-1600m
-1700m
-1800m
#66
#70
#72
#74
#81
#82
-1900m

②
-2230m
-2300m
-2400m
-2500m
#72
-2600m
#79
#82
#84
#86
#88
-2700m

③
-3400m
#169
-3500m
#175
#177
#179
#183
#185
-3600m
#195
-3700m
#216
#218
-3800m
#227
-3900m
#244
-4000m

Precambrian and Phanerozoic formations

- Quaternary sediments
- Early Cretaceous sedimentary and volcanic rocks
- UHP metamorphic rocks
- Proterozoic metamorphic rocks
- Archean metamorphic rocks

Mesozoic granitic rocks

- Early Cretaceous AiShan Cretaceous granites
- Early Cretaceous Guojialing granodiorite
- Late Jurrassic Linglong granite
- Late Triassic granitods

Veins and sample locations

- Quartz-polysulfide vein
- Quartz-pyrite vein
- Quartz vein
- Sample

Alteration rocks

- Beresitization
- Silicification
- Sericitization
- K-feldspar alteration

Deposit and fault

- Disseminated-type gold deposit
- Vein-type gold deposit
- Orebody
- Fault

Fig. 1

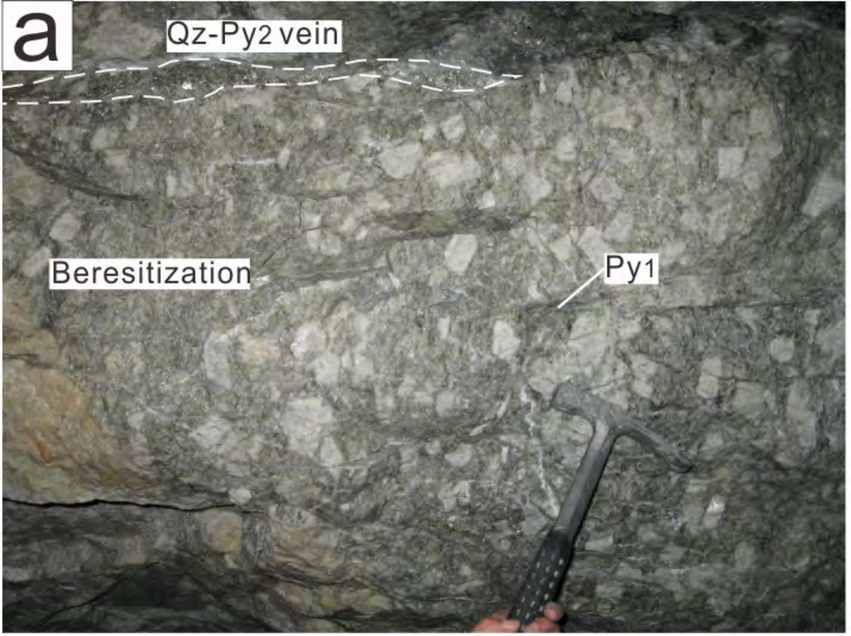
a
Qz-Py2 vein
Beresitization
Py1

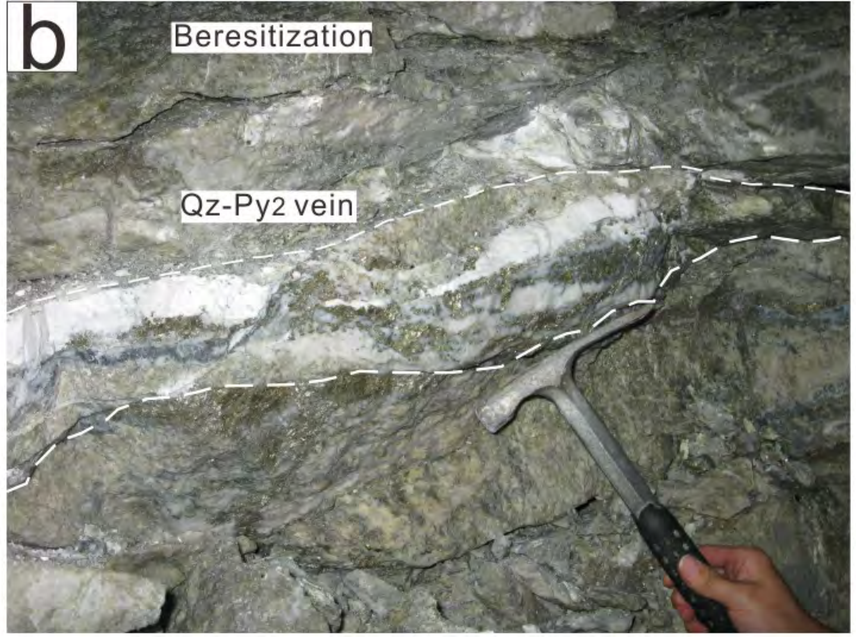
b
Beresitization
Qz-Py2 vein

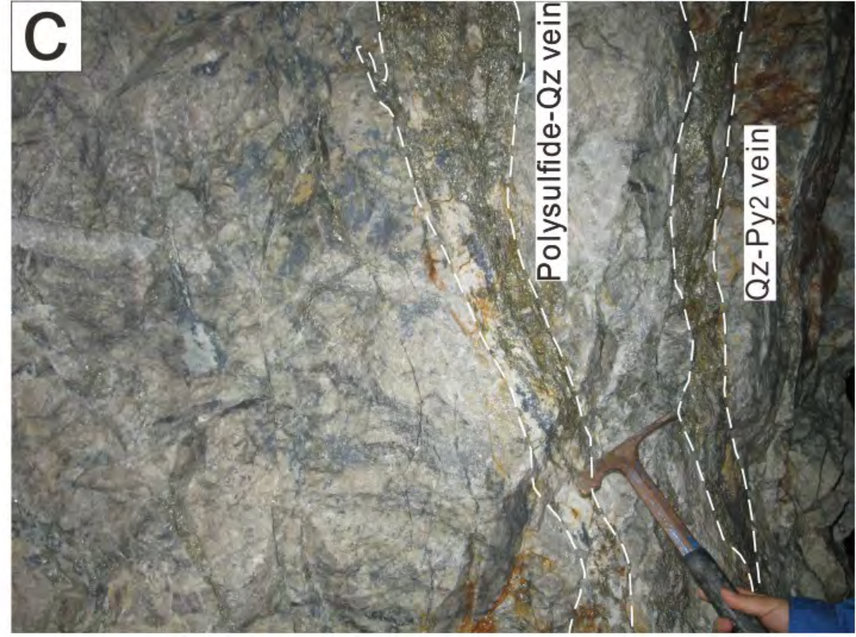
c
Polysulfide-Qz vein
Qz-Py2 vein

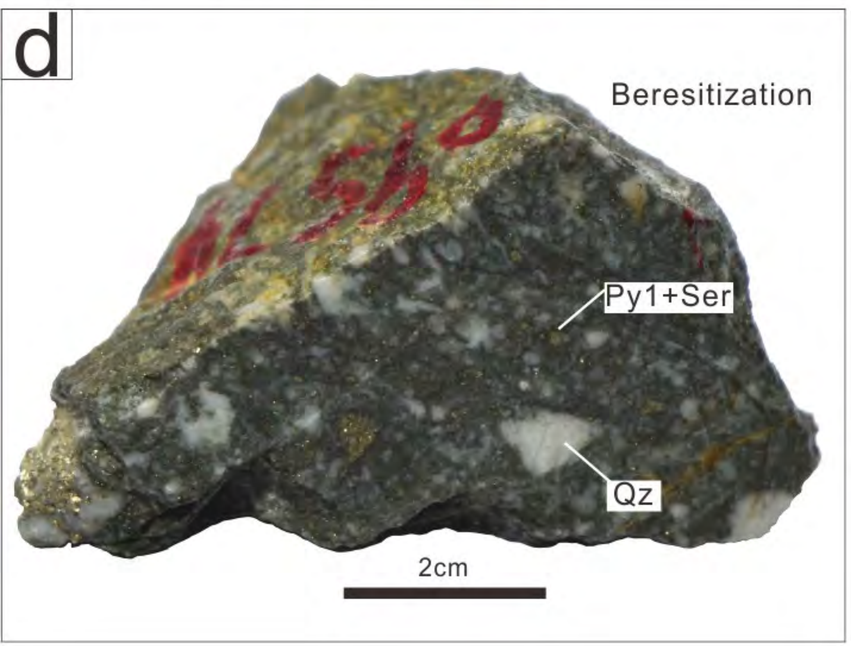
d
Beresitization
Py1+Ser
Qz
2cm

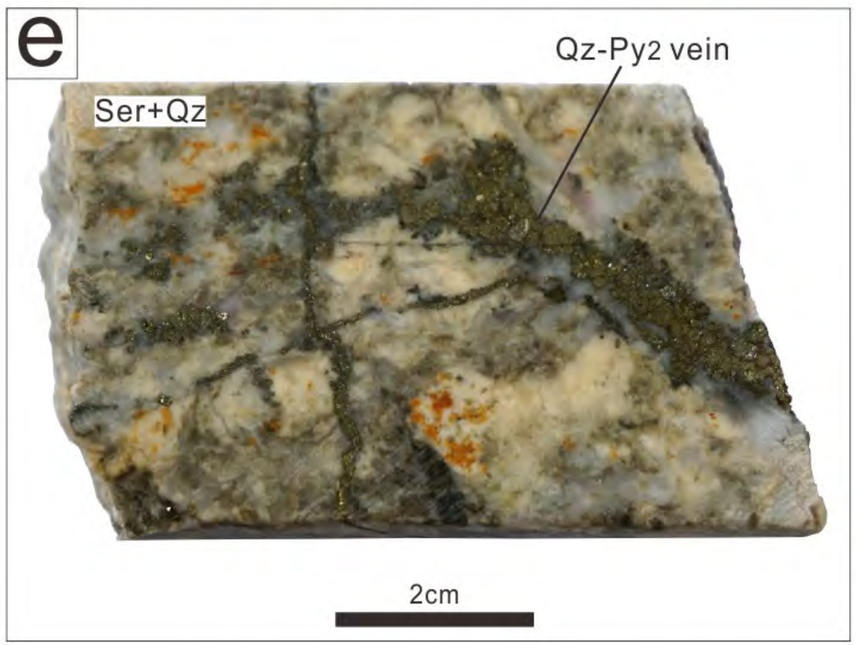
e
Qz-Py2 vein
Ser+Qz
2cm

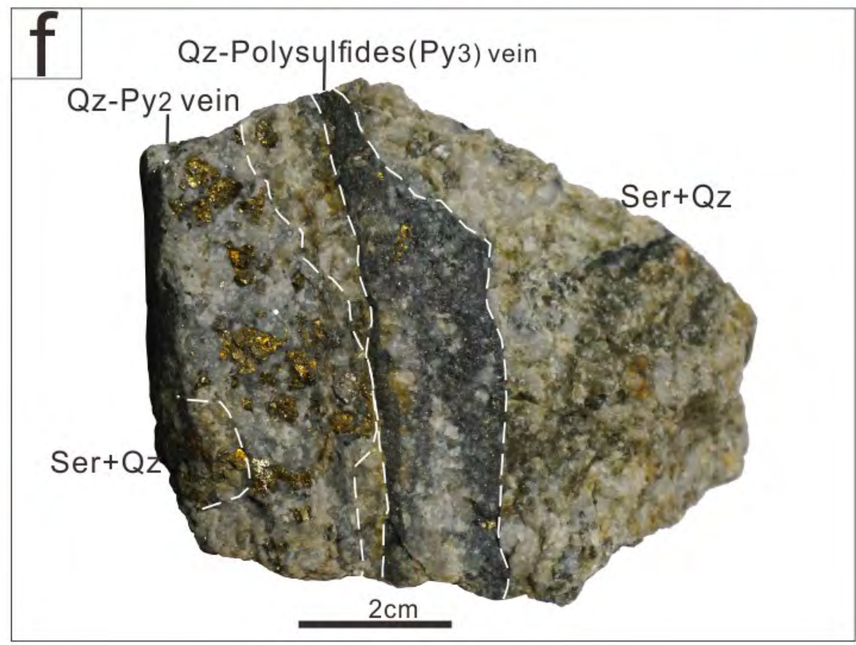
f
Qz-Polysulfides(Py3) vein
Qz-Py2 vein
Ser+Qz
Ser+Qz
2cm

Fig. 2

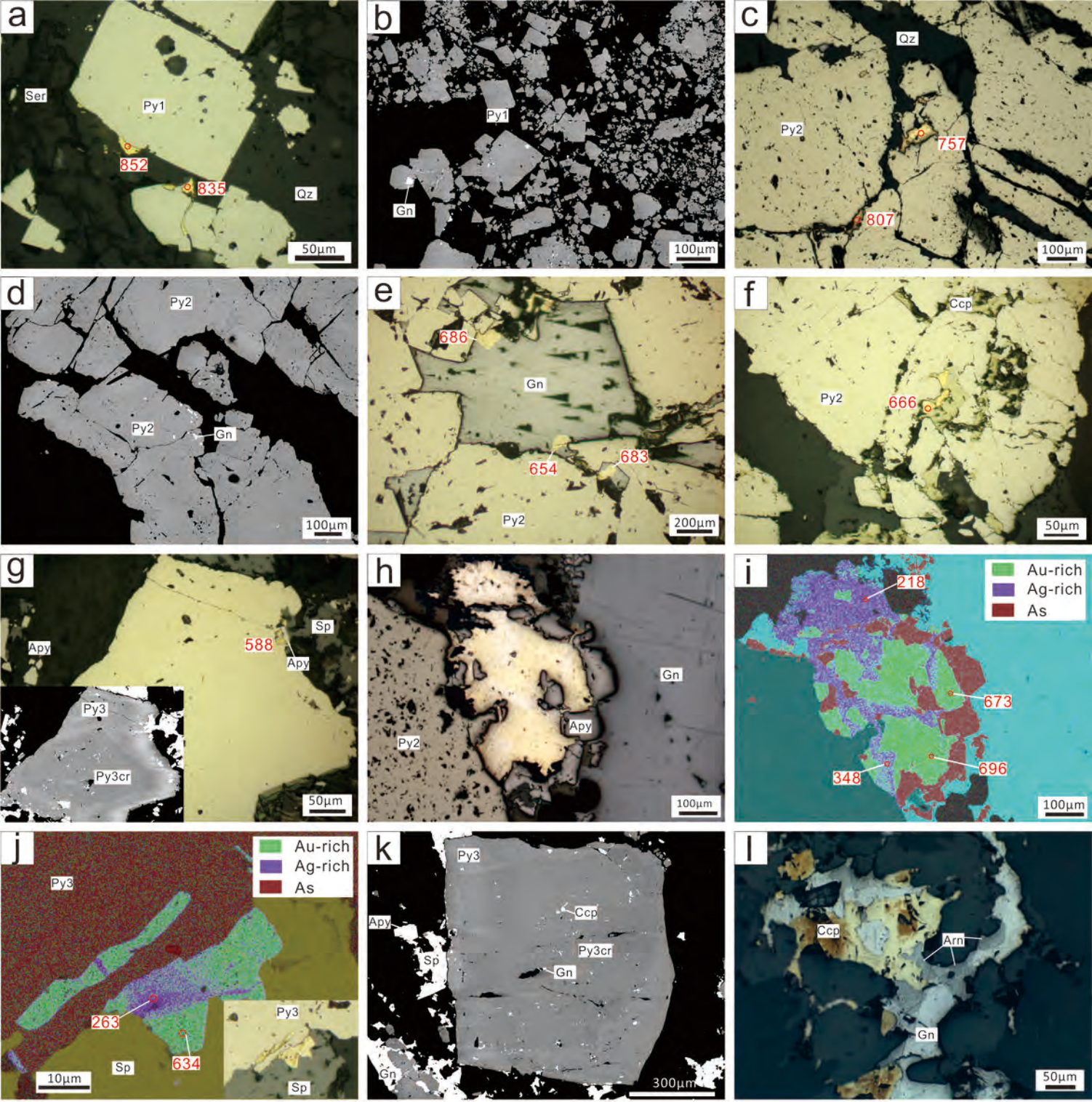
a
Ser
Py1
852
835
Qz
50μm
b
Py1
Gn
100μm
c
Qz
Py2
757
807
100μm
d
Py2
Py2
Gn
100μm
e
686
Gn
654
683
Py2
200μm
f
Ccp
Py2
666
50μm
g
Apy
588
Sp
Apy
Py3
Py3cr
50μm
h
Gn
Apy
Py2
100μm
i
Au-rich
Ag-rich
As
218
673
348
696
100μm
j
Au-rich
Ag-rich
As
Py3
263
634
Sp
10μm
Py3
Sp
k
Py3
Ccp
Apy
Sp
Py3cr
Gn
Gn
300μm
l
Ccp
Arn
Gn
50μm

Fig. 3

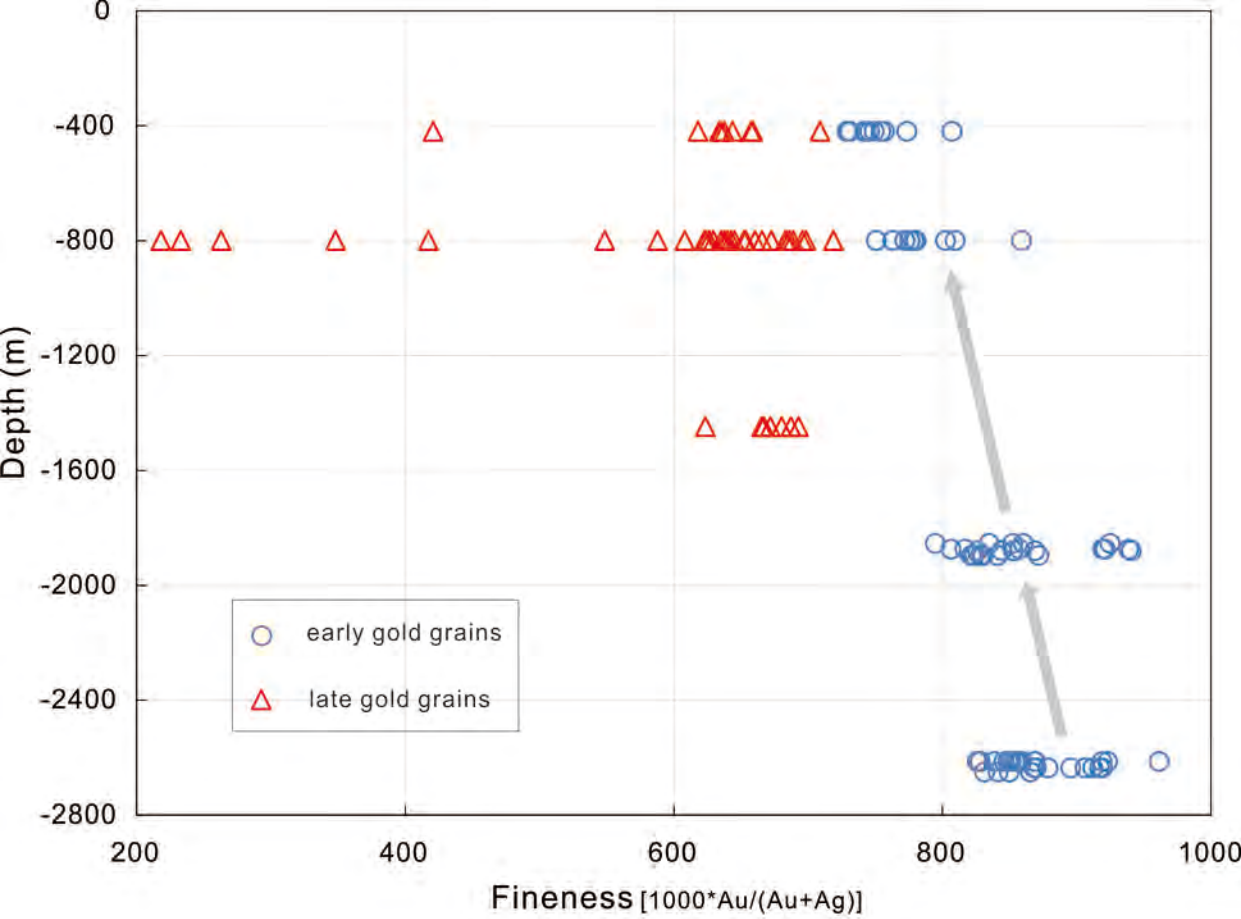
0
-400
-800
-1200
-1600
-2000
-2400
-2800
Depth (m)
200
400
600
800
1000
Fineness [1000*Au/(Au+Ag)]
early gold grains
late gold grains

Fig. 4

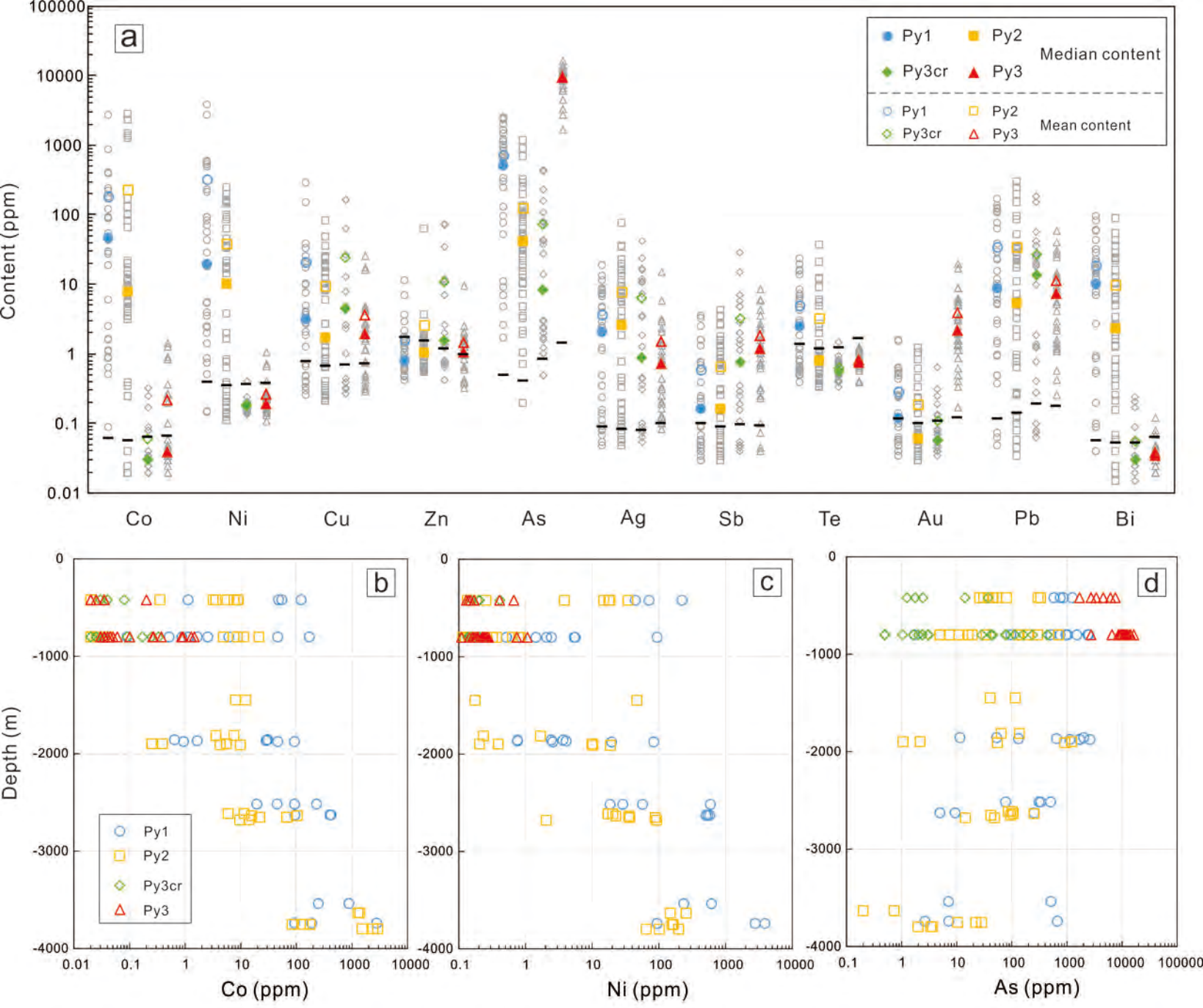
a
Py1
Py2
Py3cr
Py3
Median content
Mean content
Content (ppm)
100000
10000
1000
100
10
1
0.1
0.01
Co
Ni
Cu
Zn
As
Ag
Sb
Te
Au
Pb
Bi
b
c
d
Depth (m)
0
-1000
-2000
-3000
-4000
Co (ppm)
Ni (ppm)
As (ppm)
0.01
0.1
1
10
100
1000
10000
100000

Fig. 5

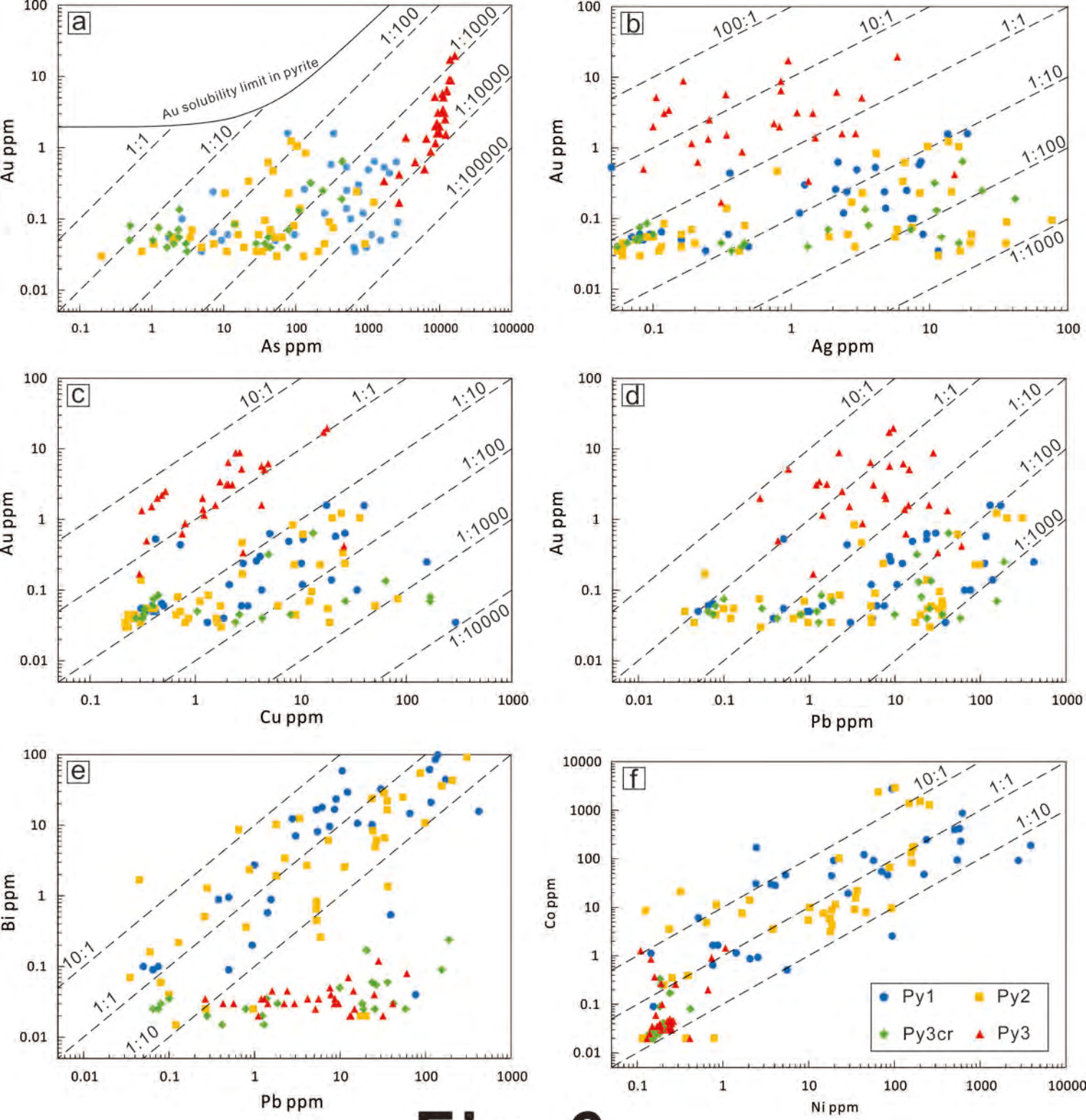
a
Au solubility limit in pyrite
1:1
1:10
1:100
1:1000
1:10000
1:100000
Au ppm
As ppm
b
100:1
10:1
1:1
1:10
1:100
1:1000
Au ppm
Ag ppm
c
10:1
1:1
1:10
1:100
1:1000
1:10000
Au ppm
Cu ppm
d
10:1
1:1
1:10
1:100
1:1000
Au ppm
Pb ppm
e
10:1
1:1
1:10
Bi ppm
Pb ppm
f
10:1
1:1
1:10
Co ppm
Ni ppm
Py1
Py2
Py3cr
Py3

Fig. 6

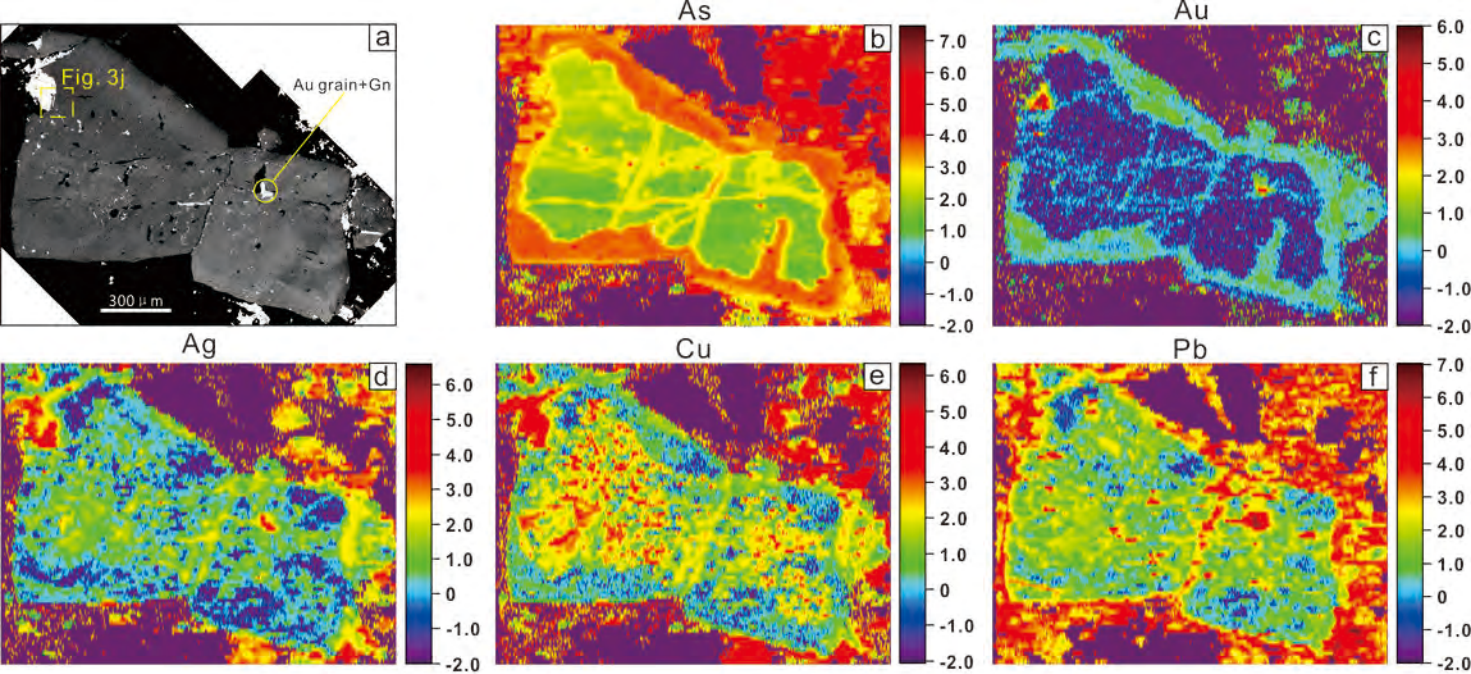
a
Fig. 3j
Au grain+Gn
300 μm
As
b
7.0
6.0
5.0
4.0
3.0
2.0
1.0
0
-1.0
-2.0
Au
c
6.0
5.0
4.0
3.0
2.0
1.0
0
-1.0
-2.0
Ag
d
6.0
5.0
4.0
3.0
2.0
1.0
0
-1.0
-2.0
Cu
e
6.0
5.0
4.0
3.0
2.0
1.0
0
-1.0
-2.0
Pb
f
7.0
6.0
5.0
4.0
3.0
2.0
1.0
0
-1.0
-2.0

Fig. 7

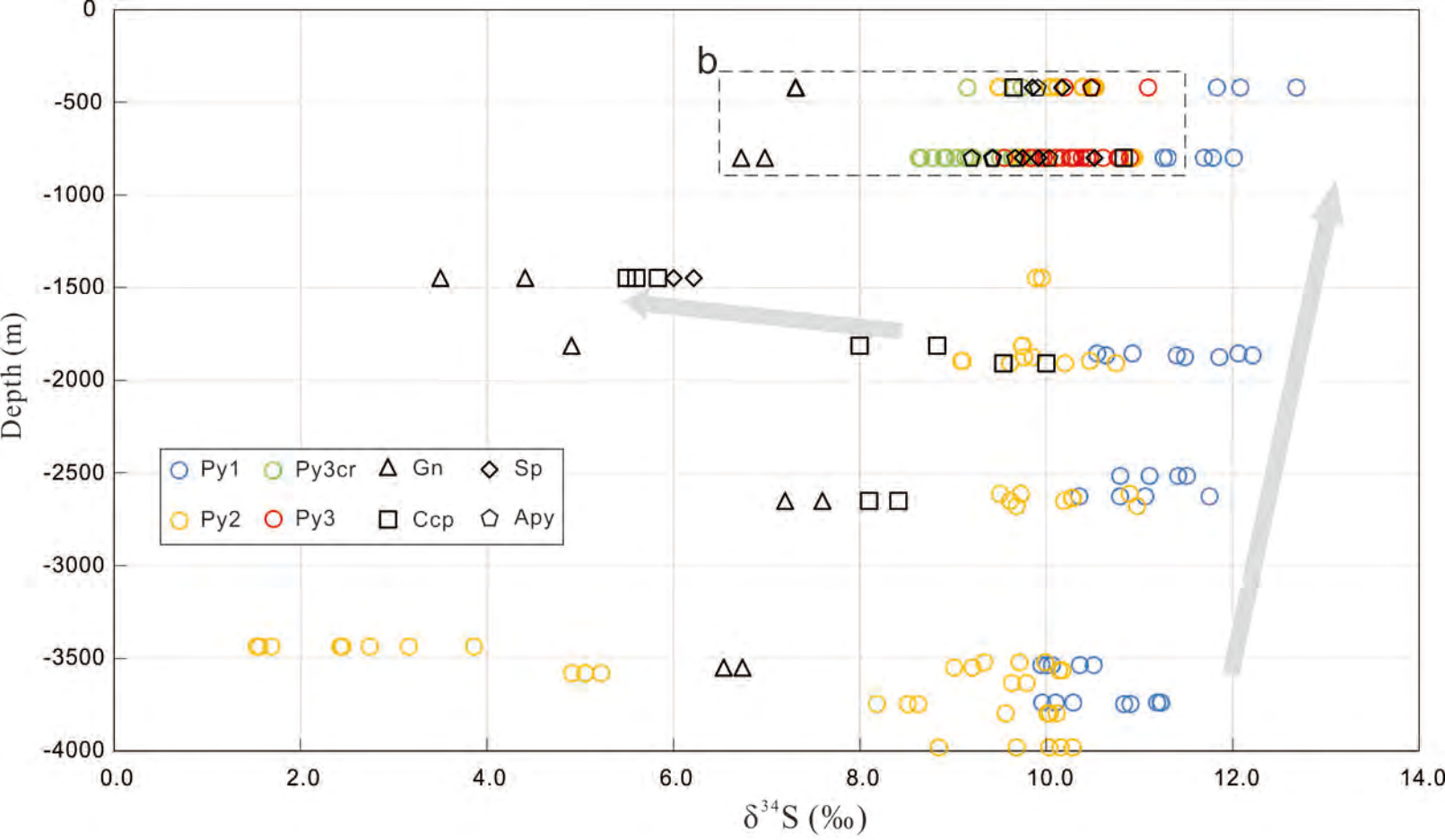
b
Py1
Py3cr
Gn
Sp
Py2
Py3
Ccp
Apy
Depth (m)
0
-500
-1000
-1500
-2000
-2500
-3000
-3500
-4000
0.0
2.0
4.0
6.0
8.0
10.0
12.0
14.0
δ34S (‰)

Fig. 8

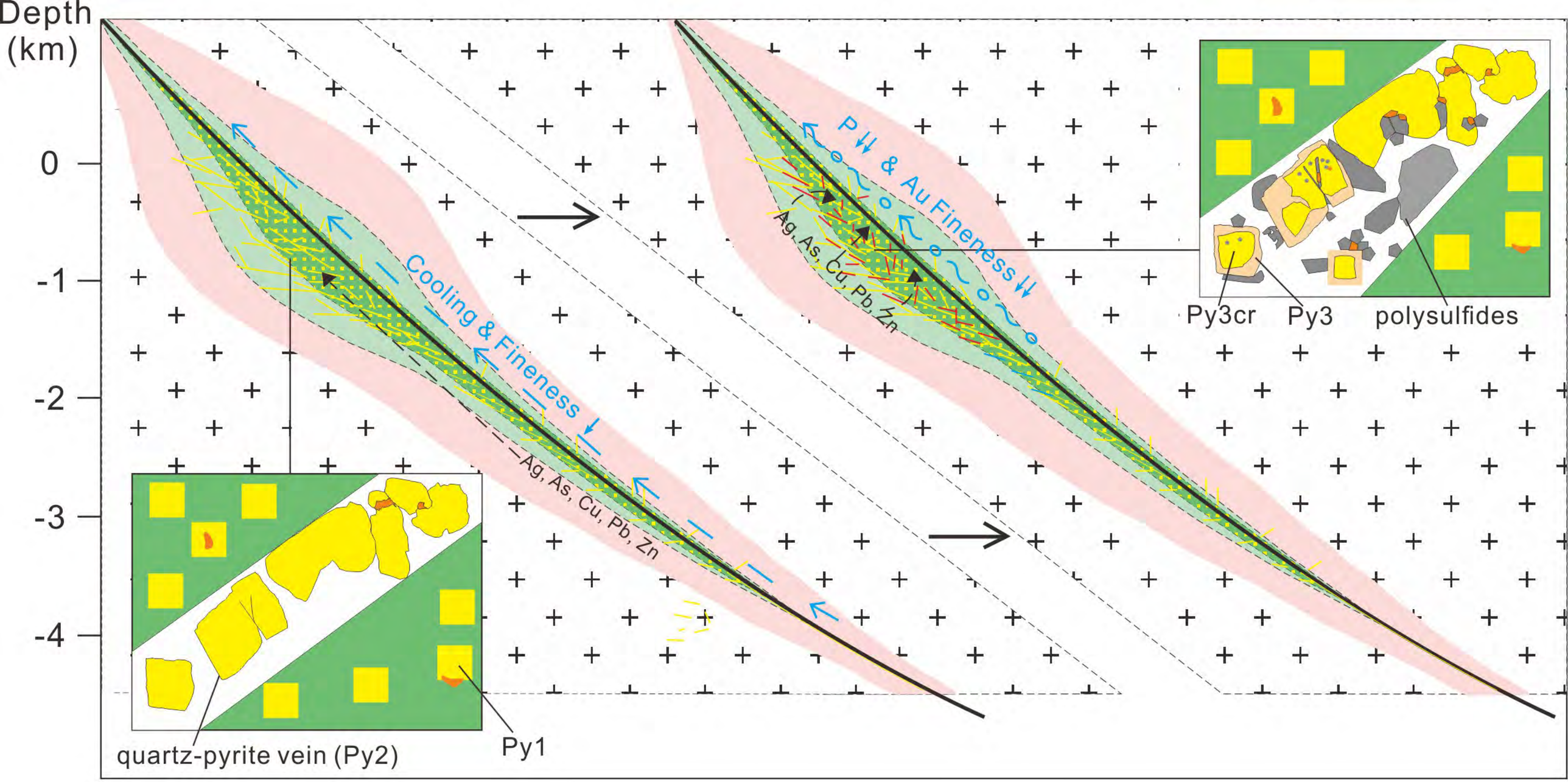

Granite

K-feldspar alteration

Sericitization

Beresitization

Fault

Single-phase fluid migration

phase separation of fluid

Quartz-pyrite vein

Quartz-polysulfide vein

Gold grain

Fig. 9